HHS Public Access

Author manuscript

Cancer Treat Res. Author manuscript; available in PMC 2015 July 07.

Published in final edited form as:

Cancer Treat Res. 2015 ; 166: 51–83. doi:10.1007/978-3-319-16555-4_3.

Theranostic Magnetic Nanostructures (MNS) for Cancer

Vikas Nandwana

Department of Materials Science and Engineering, Northwestern University, Evanston, USA

Mrinmoy De

Department of Chemistry, Indian Institute of Science, Bengaluru, India

Shihyao Chu

Sandia National Laboratory, Albuquerque, USA

Manish Jaiswal

Department of Biomedical Engineering, Texas A&M University, College Station, USA

Matt Rotz

Departments of Chemistry, Molecular BioSciences, Neurobiology, Biomedical Engineering, and Radiology, Northwestern University, Evanston, USA

Thomas J. Meade

Departments of Chemistry, Molecular BioSciences, Neurobiology, Biomedical Engineering, and Radiology, Northwestern University, Evanston, USA

Vinayak P. Dravid

Department of Materials Science and Engineering, Northwestern University, Evanston, USA v-dravid@northwestern.edu

Abstract

Despite the complexities of cancer, remarkable diagnostic and therapeutic advances have been made during the past decade, which include improved genetic, molecular, and nanoscale understanding of the disease. Physical science and engineering, and nanotechnology in particular, have contributed to these developments through out-of-the-box ideas and initiatives from perspectives that are far removed from classical biological and medicinal aspects of cancer. Nanostructures, in particular, are being effectively utilized in sensing/diagnostics of cancer while nanoscale carriers are able to deliver therapeutic cargo for timed and controlled release at localized tumor sites. Magnetic nanostructures (MNS) have especially attracted considerable attention of researchers to address cancer diagnostics and therapy. A significant part of the promise of MNS lies in their potential for “theranostic” applications, wherein diagnostics makes use of the enhanced localized contrast in magnetic resonance imaging (MRI) while therapy leverages the ability of MNS to heat under external radio frequency (RF) field for thermal therapy or use of thermal activation for release of therapy cargo. In this chapter, we report some of the key developments in recent years in regard to MNS as potential theranostic carriers. We describe that the r_2 relaxivity of MNS can be maximized by allowing water (proton) diffusion in the vicinity of MNS by polyethylene glycol (PEG) anchoring, which also facilitates excellent fluidic stability in

Correspondence to: Vinayak P. Dravid.

various media and extended in vivo circulation while maintaining high r_2 values needed for T_2-weighted MRI contrast. Further, the specific absorption rate (SAR) required for thermal activation of MNS can be tailored by controlling composition and size of MNS. Together, emerging MNS show considerable promise to realize theranostic potential. We discuss that properly functionalized MNS can be designed to provide remarkable in vivo stability and accompanying pharmacokinetics exhibit organ localization that can be tailored for specific applications. In this context, even iron-based MNS show extended circulation as well as diverse organ accumulation beyond liver, which otherwise renders MNS potentially toxic to liver function. We believe that MNS, including those based on iron oxides, have entered a renaissance era where intelligent synthesis, functionalization, stabilization, and targeting provide ample evidence for applications in localized cancer theranostics.

Keywords

Magnetic nanostructures; Theranostics; Thermal activation; MR imaging; T_2 contrast agents

1 Introduction

Magnetic nanostructures (MNS) have emerged as promising functional probes for simultaneous diagnostics and therapeutics (theranostic) applications. The diagnostics potential of MNS arises from their role in enhancing the contrast in magnetic resonance imaging (MRI). The therapeutic prospects of MNS stem from thermal activation under external applied radio frequency (RF) field and/or localized release of therapeutic cargo, either through diffusive processes or triggered by thermal activation. Both of these attributes of MNS are related to their unique size-dependent physical properties as well as compatibility of size to typical biomolecules (Fig. 1) [1–7]. The characteristics of MNS are typically measured by saturation magnetization (M_s), remanent magnetization (M_r), and coercivity (H_c). Saturation magnetization is the maximum magnetization value of MNS under an applied magnetic field while remanent magnetization is the magnetization after removing that field. Coercivity is the strength of the applied magnetic field that is necessary to reverse the remanent magnetization back to zero [8]. Superparamagnetism (SPM) occurs when particles are small enough for thermal fluctuations to cause random flipping of magnetic moments, resulting in no remanent magnetization and coercivity in the absence of an applied magnetic field, akin to para-magnetism. However, under external applied magnetic field, the nanostructures can be magnetized and manipulated for transport and thermal activation. The superparamagnetic nanostructures are essential for biomedical studies where no remanent magnetization is critical in preventing their coagulation and sustaining a long period of circulation in the body. Additional properties of MNS required for biomedicine include greater magnetic susceptibility and high saturation magnetization that results in faster and stronger response, even at low external applied magnetic field, and also enhances thermal activation. The magnetic properties of MNS are dictated by the composition, size, shape, and surface properties [9]. Hence, tuning control of these physical properties is essential for success of MNS for in vivo platform.

Typically, MNS comprise a magnetic core and biocompatible coating and/or surface functionalization that allows integration of targeting agents and bio/chemotherapeutics (Fig. 2). Targeting agents have been coupled with MNS for both diagnostic imaging and therapy of specific tumors [5, 10–12]. The diagnostic applications of MNS stem from the MRI [13]. MRI offers clinicians the ability to noninvasively obtain anatomic and metabolic/functional information with high spatial and temporal resolution [13–15]. The technique is based on the response of water proton spin in the presence of an applied magnetic field when triggered with a RF pulse. When external magnetic field is applied, protons align in one direction. Application of the RF pulse perturbs the alignment and the protons relax to the original state via two independent relaxation processes: longitudinal (T_1) and transverse (T_2) relaxation that are used to generate the MR images. The difference in water concentration and local environment between organs and tissues results in intrinsic contrast in MR images.

The spatial resolution as well as the sensitivity (S/N) of the MR images can be enhanced with the use of contrast agents. Paramagnetic molecular complexes, such as Gd(III) chelates, are used as T_1 contrast agents that increase signal intensity, i.e., higher r_1 relaxation, and appear bright in T_1-weighted images [16]. T_1 contrast agents are not covered in this chapter, however, a number of recent reviews have appeared [15–20]. MNS are used as T_2 contrast agents that decrease the signal intensity, i.e., higher r_2 relaxation, and appear dark in T_2-weighted images. When water molecules (protons, more specifically) diffuse into the periphery of the induced dipole moment by MNS, the T_2 relaxation time of the protons is shortened, which enhances the negative contrast that helps in differentiating between pathogenic targets and normal tissues in T_2 weighted MRI images (Fig. 3).

Several MNS-based T_2 contrast agents (e.g., Feridex and Resovist) have been clinically approved [21, 22]. The MRI contrast enhancement effect is measured by the relaxation rate R_1 (s^{-1}) and the relaxivity coefficient r_2, a slope of R_2 against MNS concentration. The R_2 relaxation rate of MNS is defined as

$$R_2=\frac{1}{T_2}=\frac{256\pi^2\gamma^2}{405}M_s^2V\frac{r^2}{D\left(1+\frac{L}{r}\right)} \quad (1)$$

where T_2 is transverse relaxation time, γ is proton gyromagnetic ratio, M_s is saturation magnetization, V is volume of MNS, D is diffusion coefficient of water molecules, r is radius of MNS core, and L is thickness of MNS surface coating. [23]. The higher relaxivity corresponds to a better contrast effect. Based on Eq. (1), MNS should have high magnetization (M_s), large volume (V), and thin surface coating (small L) for better contrast effect.

MNS can generate heat under external RF field that make them very useful in cancer therapeutics. Under an external RF field (typically a few hundred kHz), superparamagnetic MNS switch their magnetization direction along the field directions, back and forth. The frictions caused by the physical rotation of the MNS (Brownian relaxation) and the magnetization reversal within the MNS (Neel relaxation) lead to the loss of magnetic energy and the generation of thermal energy [24]. The capability of generating heat at any targeted areas can be used for directly killing cancer cells via the thermal therapy and/or as an

actuator for bio/chemo therapy cargo release. The thermal activation of MNS is measured by the specific absorption rate (SAR) that is measured as the initial temperature rise of the MNS solution per unit volume or mass.

$$SAR = \pi \mu_0 \chi_0 H_0^2 f \frac{2\pi f \tau}{1+(2\pi f \tau)^2} \quad (2)$$

where μ_0 is vacuum permeability, χ_0 is equilibrium susceptibility, H_0 is RF field amplitude, and f is frequency of the external RF field. The higher *SAR* is crucial for clinical use since that would require a smaller amount of MNS to be injected into the patient. According to Eq. (2), SAR highly depends on various parameters such as the size, size distribution, shape, chemical composition and surface modification, and saturation magnetization of the particles [25]. In addition, it is clear that SAR values depend on the frequency f and the field amplitude H_0 of the applied field. However, in order to apply hyperthermia safely to patients and avoid any detrimental effect on healthy tissues due to electromagnetic radiation exposure, the $H_0 f$ factor should not exceed a threshold that was experimentally estimated to equal 5×10^9 A m^{-1} s^{-1} [26]. Therefore, MNS with an exceptional SAR value that can generate heat under $H_0 f$ limit is highly desirable.

2 Synthesis and Characteristics of MNS: Prospects for Theranostics

For successful theranostic applications, MNS should be monodispersed and have uniform composition because the magnetic properties of MNS depend on the size, shape, and composition. It is clear from Eqs. (1) and (2) that the particles should possess high saturation magnetization and magnetic susceptibility, and be stable to a range of pH and salt concentrations. A key parameter for the magnetization of MNS is size. In a bulk magnetic material, all of the magnetic spins are aligned parallel to the applied magnetic field. However, in the nanoscale regime, a magnetically disordered spin-glass-like surface layer is formed. As the nanoparticle size decreases, such surface spin-canting effect becomes more pronounced and causes a drop in the saturation magnetization. While high saturation can be achieved with larger size particles, avoiding the surface-canting effect [27], the particle size should be under the superparamagnetic limit, which is typically less than ~20–30 nm for the majority of MNS. Further, the particles should have a coating or surface functional moieties that improve dispersion, biocompatibility, and provides a surface that can be functionalized. Strict attention to these parameters is essential during the design, synthesis, and formulation of MNS in order to be useful for in vivo applications.

MNS can be fabricated by either top-down (mechanical attrition) or bottom-up (chemical synthesis) approaches [9]. Since magnetic properties change with size and composition of MNS, chemical routes are preferred since they can synthesize MNS with uniform composition and size. The chemical methods include co-precipitation, microemulsion, thermal decomposition and/or reduction, hydrothermal synthesis, and polyol synthesis. Two excellent reviews describing MNS fabrication methods have recently appeared and we will provide only a brief summary here [28, 29].

The most common synthetic strategy involves aqueous precipitation of iron salts with in situ, or post-synthesis addition of surfactant [30]. This strategy has notable limitations

yielding monodispersity [31]. The microemulsion method does produce MNS of narrower size distribution compared to aqueous precipitation, but suffers from low yields [32]. Recently, the thermal decomposition/reduction method has gained considerable attention since this technique offers fine control over the final particle size, shape, and crystal structure compared to other methods and is scalable [33, 34]. Monodispersed MNS are formed due to the reaction conditions that yield a quick nucleation step followed by slower growth phase. However, the reaction occurs in organic solvent containing hydrophobic stabilizers, which requires additional surface modifications to the MNS to impart aqueous stability.

Here, we discuss different types of MNS synthesized using chemical methods and their magnetic properties. Table 1 summarizes different MNS core materials, their magnetic properties, and r_2 relaxivity.

2.1 Ferrite MNS

Fe_3O_4 MNS are extensively used in biomedicine because of their biocompatibility and ease of synthesis [47, 48]. The magnetic moment of superparamagnetic Fe_3O_4 MNS is dependent on the size with smaller particles producing lower magnetic moments [49]. Hence, the size of Fe_3O_4 MNS can be tuned by changing the reaction conditions such as reflux temperature, reflux time, and heating rate. The magnetic moment of Fe_3O_4 MNS was tuned from 25 to 43, 80, and 102 emu/(g Fe) with change in the size from 4, 6, 9, and 12 nm, respectively (resulting in r_2 values of 78, 106, 130, and 218 mM^{-1} s^{-1}) [27]. Further, the magnetic moment of Fe_3O_4 MNS can be modified by doping transition divalent metal ions (Co^{2+}, Ni^{2+}, Mn^{2+}, and Zn^{2+}). By adding different metal precursors during Fe_3O_4 synthesis, monodisperse MFe_2O_4 MNS were synthesized [38]. The metal ferrite nanostructures have an inverse spinel crystal structure composed of face-centered cubic packed lattice of oxygen atoms with octahedral sites (O_h) occupied by Fe^{3+} and M^{2+} ions and tetrahedral sites (T_d) occupied by Fe^{3+} ions (Fig. 4a). The magnetic spins of the ions at the O_h and T_h sites align opposite to each other. Hence the spins of Fe^{3+} ions at O_h and T_h cancel each other and net magnetization of MFe_2O_4 MNS is decided by magnetic moment of M^{2+} ions (Fig. 4b). The magnetization of $NiFe_2O_4$, $CoFe_2O_4$, Fe_3O_4, and $MnFe_2O_4$ were found to be 85, 99, 101, 110 (emu/g metal ions), respectively, depending upon the magnetic moments of the M^{2+} ions. This resulted in r_2 values of 152, 172, 218, and 358 mM^{-1} s^{-1} (Fig. 4c) [38].

Interestingly, doping of nonmagnetic Zn in Fe_3O_4 and $MnFe_2O_4$ MNS resulted in $(Zn_xFe_{1-x})Fe_2O_4$ and $(Zn_xMn_{1-x})Fe_2O_4$ MNS, respectively, that exhibit extremely high net magnetic moment and r_2 relaxivity [42]. The magnetization of $(Zn_xMn_{1-x})Fe_2O_4$ was dependent on the Zn doping level and were found to be 125, 140, 154, 166, 175, and 137 emu/g metal ions for x = 0, 0.1, 0.2, 0.3, 0.4, and 0.8, respectively, resulting in the r_2 values of 422, 516, 637, 754, 860, and 388 mM^{-1} s^{-1}, respectively (Fig. 5). The r_2 value for $Zn_{0.4}Mn_{0.6}Fe_2O_4$ MNS is the maximum r_2 value of reported to date for MNS [42], eight times higher than r_2 of Feridex [36]. $(Zn_xFe_{1-x})Fe_2O_4$ MNS exhibited a similar trend, but the magnetization and r_2 values were slightly lower than $(Zn_xMn_{1-x})Fe_2O_4$ MNS (Fig. 5) [42].

2.2 Metallic MNS

MNS based on transition metals of Fe, Co, Ni, and their alloys have higher magnetic moments than their oxide counterparts [44, 50–53]. Saturation magnetization of bulk FeCo (240 emu/g) and Fe (218 emu/g) is particularly high compared to bulk Fe_3O_4 (90 emu/g). Using the same mass of metallic MNS would then produce a far greater impact than their oxide counterparts, improving the T_2 contrast enhancement and therapeutic efficacy of drug delivery. However, the metallic MNS carries their own set of disadvantages like chemical instability, leaching of the noniron elements, and toxicity that renders them questionable for in vivo applications [9, 53, 54]. In addition, these pure metal nanoparticles are also ferromagnetic at room temperature, rather than superparamagnetic. This means that once they are magnetized, they will remain that way regardless of whether an external magnetic field is withdrawn, resulting in an aggregation. A number of reports have been published demonstrating coatings that prevent aggregation and ensure chemical stability of metallic MNS. Options under consideration include inert metals, such as Au and Ag, peptide capping ligands, ferrites, graphite, and silica [43, 44, 52, 55–57]. For example, after graphitic shell coating, FeCo MNS were stable up to 1 month and showed very high magnetic moment (215 emu/g) and r_2 relaxivity (644 mM^{-1} s^{-1} which is far superior to conventional ferrite MNS [43, 52]. Crystalline Fe_3O_4 shell was also used to protect metallic Fe MNS that resulted in M_s and r_2 of 164 emu/g and 220 mM^{-1} s^{-1}, respectively [44, 56]. Co MNS were coated with Au shell to provide an inert, biocompatible and stable shell with a well-known surface chemistry. Though the bulk saturation magnetization of Co is ~160 emu/g, the measured value was found ~100 emu/g after Au coating, which was still higher than Fe_3O_4 MNS (75–80 emu/g) [55].

2.3 Multifunctional MNS

Hybrid MNS with two or more different functional units, such as Au–Fe_3O_4, FePt–CdS, and Fe_2O_3–carbon nanotube can be synthesized through seed mediated growth. In such a heterogeneous nanostructure, each unit exhibits its unique magnetic, optical, or electronic properties [10, 58–60]. Au–Fe_3O_4 nanostructures were prepared that preserved the optical property of Au (plasmonic absorption at ~530 nm) as well as the magnetic property of Fe_3O_4 MNS (M_s = 80 emu/g) [61]. This approach was extended to prepare semiconductor-metal alloy [62], semiconductor–metal oxide [63], and carbon nanotube–metal oxide complex [64]. MNS have been coupled with a wide range of fluorophores for multimodal imaging applications [65–67]. Lastly, T_1/T_2 MRI agent were prepared by conjugating Gd (III) based chelating agent with MNS [68].

3 Coating and Functionalization of MNS

In order to apply MNS in vitro and subsequently in vivo, the surface needs to be functionalized so that it; (i) protects against agglomeration; (ii) provides biocompatibility and chemical handles for the conjugation of drugs and targeting ligands; (iii) limits nonspecific cell interactions; and (iv) enhances MNS pharmacokinetics [69]. A diverse group of organic and inorganic coatings has been investigated including DMSA [27], PEG [70, 71], dextran [72], chitosan [73], liposomes [74], gold [75], and silica [76]. MNS coating can be achieved via a number of approaches, including in situ coating, post-synthesis

adsorption, and post-synthesis end grafting [15]. Here, we discuss some of the most common coatings, their methods of attachment, and examples in cancer targeting.

3.1 Poly(Ethylene Glycol) (PEG)

PEG is a neutral and amphiphilic polymer that has been used clinically as excipients in FDA approved pharmaceutical formulations [77]. PEG coating of MNS improves their dispersion in biological media and increases blood circulation time since they are not readily recognized by the reticuloendothelial system (RES) [78]. Lutz et al. demonstrated in situ coating of PEG onto Fe_3O_4 MNS under aqueous conditions [79] while PEG grafting was achieved by single-point chemical anchoring through different functional groups including silanes [70], phosphate derivatives [80] and dopamine [81]. Peng and Sun reported ligand exchange with bifunctional PEG with dopamine [56]. Most recently, nitrodopamine has been proposed as an ultrastable chemical anchor for MNS [82]. We have developed MNS with high buffer stability by coating Fe_3O_4 with bifunctional PEG conjugated with nitrodopamine and carboxylate terminal groups [83]. The nirodopamine was covalently attached to the Fe_3O_4 surface by one end and the carboxylate group at the other end was kept open to functionalize with targeting ligands or therapeutic agents.

3.2 Dextran

Dextran is a branched polysaccharide comprised of glucose subunits and is widely used for MNS coatings because of its biocompatibility and polar interactions (chelation and hydrogen bonding). Addition of dextran during synthesis of Fe_3O_4 via the co-precipitation method resulted in dextran coated Fe_3O_4 MNS [84]. Subsequent iterations of this method produced clinically approved ferumoxtran-10 (AMI-277) and ferumoxides (AMI-25) [85–90]. These two structures have cores of ~5 nm, but differ significantly in dextran coating thickness (20–40 nm vs. 80–150 nm) which results in varying blood circulation times (24 h for ferumoxtran and 2 h for ferumoxides) [35]. Since the dextran molecules are adhered nonspecifically through hydroxyl interactions with the iron oxide core, there is always a possibility of desorption [91]. In order to prevent this, the dextran polymers were chemically cross-linked on MNS surface [92]. Using this strategy, clinically approved ferumoxytol [93] and ferucarbotran [22] have been synthesized.

3.3 Silica

Silica coating on MNS is popular because of the ease of synthesis and aqueous stability. By hydrolyzing silica precursors in basic solution, a uniform and thickness-controllable silica coating on MNS was obtained [76, 94, 95]. The silica shell have been used as a carrier for anticancer drugs (e.g., paclitaxel) and fluorescent molecules (e.g., fluorescein isothiocyanate (FITC)) [96]. Imparting additional functionalities to the silica coating have enabled targeting and labeling functionality. By addition of 3-aminopropyl-triethoxysilane (APS) to the silica precursors, we have coated silica shells with primary amine groups with controlled thickness [97]. Similarly, by reacting APS with isothiocyanate functionalized fluorescent dyes, Lu et al. were able to develop fluorescent MNS, a multimodal diagnostic agent [94]. Currently, silica coated MNS is available as ferumoxil (AMI-121), an orally ingested T_2 contrast agent for delineation of the intestinal loops from adjacent tissues and organs [21].

4 Pharmacokinetics and Biodistribution

The two most important factors that determine MNS pharmacokinetics are their surface characteristics and hydrodynamic size [98, 99]. Interplay of these properties with the reticuloendothelial system (RES) clearance determines plasma lifetime (blood circulation time). In RES clearance, circulating opsonin proteins adsorb to MNS surface (opsonization) that are recognized and removed from the bloodstream by tissue macrophages (Fig. 6). It has been shown that MNS with a hydrodynamic diameter of 10–100 nm are pharmacokinetically optimal for in vivo applications [100]. MNS smaller than 10 nm are subject to tissue extravasation and renal clearance, whereas those larger than 100 nm are quickly opsonized and eliminated from the circulation via the RES [31]. Decuzzi et al. produced models suggesting that within this range, smaller size nanostructures have longer blood circulation time [101].

With respect to the surface properties, charge can affect pharmacokinetics of MNS by enhancing their interactions with the plasma proteins and nontargeted cells, resulting in short blood circulation time [102]. In addition, hydrophobic groups on the surface of MNS induce the agglomeration of the MNS upon injection, leading to rapid removal by the RES. The rate of clearance, however, can be reduced by modification of MNS surfaces with coatings that resist RES interactions. As mentioned, surface modification with molecules such as the hydrophilic PEG has been a hallmark solution to many pharmacokinetic problems, including MNS [103, 104]. PEG chains linked to MNS reduce opsonization and macrophage uptake processes through steric repulsion, prolonging their circulation times [78, 105].

MNS biodistribution and cell uptake is significantly influenced by their physicochemical properties [99, 106, 107]. For example, it has been reported that MNS smaller than 150 nm accumulates in the bone marrow, heart, kidney, and stomach [108] while MNS larger than 150 nm are found in the liver and spleen [109]. Villanueva et al. showed that the charge and nature of surface functionalizing molecules on MNS affected their uptake of cancer cells [110]. They found that cells had effective uptake of positively charged aminodextran-MNS, minimal uptake of neutral charged dextran coated MNS, and low uptake of negatively charged DMSA-coated MNS [110]. Chouly et al. have found that negatively charged MNS gets opsonized quicker than neutral MNS and had greater liver uptake [99].

5 Targeting of MNS to Localized Cancer Tumors

The targeting of MNS for selected tumor tissues is critical in both diagnostic imaging and therapeutics [5, 10, 11]. Since nonspecific cell binding can place healthy tissue at risk, MNS have been engineered to target tumor tissues through passive and active targeting approaches.

5.1 Passive Targeting

Passive targeting uses the predetermined physicochemical properties of MNS to specifically migrate to selected tissues. The most common example of passive targeting is the enhanced permeability and retention (EPR) effect where MNS smaller than 200 nm can accumulate in many tumor tissues passively in solid tumors [111]. The compromised vasculature of a solid

tumor facilitates passive MNS extravasation from the circulation into the tumor interstitium (Fig. 7) [112]. By contrast, endothelial cells of normal tissue vessels are closely packed and present a barrier for MNS penetration. However, passive targeting is limited to specific tumors since success of EPR effect depends on a number of factors such as lymphatic drainage rate, degree of capillary disorder, and blood flow which varies in different tumor types [113, 114].

5.2 Active Targeting with Targeting Agents

Because passive targeting is available for only certain types of tumors and does not necessarily guarantee internalization of MNS by targeted cells, MNS can be modified with tumor-selective agents to employ active targeting [115, 116]. These agents are complementary to unique receptors that are overexpressed or present on tumor cells. A variety of targeting agents have been used for MNS, depending on the specific target, and these are reviewed elsewhere [5, 10]. Some of the studies include: small organic molecules [115, 117, 118], peptides [119], proteins [120], and antibodies [27]. The density and molecular organization of these ligands significantly influence MNS binding to target cells due to the multivalency phenomenon [121]. Some of the targeting agents can be used to facilitate MNS internalization into cells, primarily via endocytosis [5]. However, synthesis of these targeting agents is expensive and involves complicated chemistry. Therefore, the process of scaling up the synthesis is challenging and may be a hurdle for clinical applications.

5.3 Active Targeting with External Magnetic Field

Accumulation of MNS can be realized by applying external magnetic field on the target site, a unique feature for MNS. Magnetic targeting has been studied for a number of tumor models [122, 123]. This technique was successfully implemented in a clinical trial to deliver the chemotherapeutic, doxorubicin, to hepatocarcinoma cells [124]. David et al. have explored magnetic targeting to brain tumors with PEI functionalized MNS [102, 122]. While successful, the efficacy of magnetic targeting is limited to target tissue that is close to the body's surface, since the magnetic field strength decreases with the distance from the magnetic source.

6 MNS for Diagnostic Imaging of Cancer

The diagnostic imaging applications of MNS have been realized as T_2 contrast agents in MR imaging over the past 20 years [13–15, 28, 125]. Owing to their significant deposition in liver, several MNS-based clinically approved T_2 contrast agents (Feridex I.V.®, Resovist®, and Gastromark®) have been used for liver imaging of humans [21, 22]. In order to extend MR visibility to image tumor at other parts, targeting agents have been coupled to MNS [85]. For example, Artemov et al. used Fe_3O_4 MNS conjugated with biotinylated Her-2/neu antibody Herceptin to generate strong T_2 contrast in breast cancer cell lines (AU-565, MCF-7, and MDA-MB-231) overexpressed with tyrosine kinase Her-2/neu receptors [126]. Contrast observed in MR images was found to be proportional to the expression level of kinase her-2/neu receptors for the given cell lines. Gao et al. successfully performed targeted MR imaging of human colon carcinoma xenograft tumors in mice by conjugating a cancer-

targeting antibody (rch 24 mAb), to an 11 nm Fe_3O_4 MNS [127]. T_2 and T_2*-weighted MR images acquired before and after injection showed that the tumor site turned dark as early as 10 min after the injection of the rch 24 mAb conjugates and became darker and bigger until 24 h. In contrast, the Fe_3O_4 MNS without rch 24 mAb showed nearly no variation after injection [127]. Sun et al. reported c(RGDyK) peptide-coated Fe_3O_4 MNS and demonstrated their in vivo tumor-specific targeting capability [128]. When administrated intravenously in a mice bearing U87MG tumors, the c(RGDyK) peptide-coated Fe_3O_4 MNS accumulated preferentially in the integrin αvβ3-rich tumor area resulting in a significant drop in the tumor MR signal intensity [128].

Other than target-specific molecular imaging, MNS-based contrast agents have been used in MRI for cell-based therapy since cells must be tracked in vivo to optimize cell therapy [129–134]. MRI-based immune cell tracking using MNS has been applied to many types of preclinical studies, such as tumor targeting of cytotoxic T cells and natural killer cells [135, 136], organ-specific targeting of autoimmune T cells [137], and neural stem cells [138]. De Vries et al. have shown that in vivo magnetic resonance tracking of MNS labeled dendritic cells is feasible in humans in conjunction with detailed anatomical information in melanoma patients. In contrast to scintigraphic imaging, MRI allowed assessment of the accuracy of dendritic cell delivery and of inter- and intranodal cell migration patterns [139–143]. Recently, Bulte et al. evaluated the long-term clinical tracking of MNS labeled stem cells after intracerebroventricular transplantation in an 18-month-old patient with global cerebral ischemia [144]. Twenty-four hours post-transplantation, MRI was able to detect hypointense cells in the occipital horn of the lateral ventricle. The signal gradually decreased over 4 months and became undetectable at 33 months.

To improve T_2 contrast for advanced MR imaging, researchers have been studying various parameters that affect the r_2 relaxivity of MNS. In the following sections, we discuss the parameters that have improved T_2 contrast of MNS for cancer diagnostic imaging. They have been divided into four categories; (i) size, shape, and composition control; (ii) nanoassembly of MNS; (iii) coating of MNS; and (iv) MNS with metal core.

6.1 Size, Shape, and Composition Control

According to Eq. 1, the R_2 of MNS is proportional to saturation magnetization and volume. Since the saturation magnetization of an MNS is proportional to its size due to surface spin-canting effects, the r_2 value of MNS can be increased by increasing the size of MNS. However, for biological imaging applications, the hydrodynamic size of MNS should be below 100 nm in order to have longer circulation times and to avoid nonspecific uptake [145]. Cheon et al. investigated the size effect where Fe_3O_4 MNS of diameter 4, 6, 9, and 12 nm resulted in the r_2 relaxivity of 78, 106, 130, and 218 mM^{-1} s^{-1}, respectively (Fig. 8). The MR contrast changed from light gray to black or from red to blue in color-coded images (Fig. 8) [27]. The 9 nm Fe_3O_4 MNS conjugated with Herceptin was used to image a breast cancer cell line, SK-BR-3, which possesses overexpressed HER2/neu cancer markers. Herceptin was selected due to its specific binding properties against a HER2/neu receptor. In the T_2-weighted MR images, treatment of 9 nm Fe_3O_4 MNS-Herceptin probe conjugates to the SK-BR03 breast cancer cell lines resulted in the significant negative contrast of the MR

images compared to nontreated cell lines [27]. Chen et al. studied the size effect of polyvinylpyrrolidone (PVP)-coated Fe_3O_4 MNS (core size 8, 23, 37, and 65) on MRI of hepatic lesions in vivo [146]. PVP-Fe_3O_4 MNS with core size 37 and 65 nm showed higher r_2 relaxivity (239 and 248 mM^{-1} s^{-1}, respectively) compared to other sizes. When administered in nude mice bearing orthotopic Huh7 liver cancer, PVP-Fe_3O_4 MNS with 37 nm core size showed higher contrast change compared to Feridex in T_2 and T_2* weighted MR images [146].

The change in shape of the MNS has been used to increase r_2 relaxivity. We reported size and shape effects of $CoFe_2O_4$ MNS on their r_2 relaxivity. Spherical $CoFe_2O_4$ MNS of various sizes were synthesized via seed mediated growth method, while faceted irregular $CoFe_2O_4$ MNS were synthesized via the same method but in the presence of a magnetic field [147]. While the r_2 relaxivity coefficient of $CoFe_2O_4$ MNS increased with an increase in size for spherical particles, faceted $CoFe_2O_4$ MNS showed higher r_2 relaxivity than spherical $CoFe_2O_4$ MNS [147]. Recently, Gao et al. reported octapod shape Fe_3O_4 MNS that exhibited highest relaxivity of 679.3+/30 mM^{-1} s^{-1} for Fe_3O_4 and demonstrated in vivo imaging and tumor detection [148].

As discussed earlier, the magnetization (and hence r_2) of MNS can be influenced by doping with magnetically susceptible elements. The effect of metal doping on the r_2 relaxivity was investigated for MFe_2O_4 in which Fe^{2+} ions were replaced by other transition metal dopants (Mn^{2+}, Zn^{2+}, Ni^{2+}, and Co^{2+}). The r_2 of 12 nm $MnFe_2O_4$ MNS was observed 358 mM^{-1} s^{-1} compared to 218 and 62 mM^{-1} s^{-1} from 12 nm Fe_3O_4 and dextran coated cross-linked 4 nm Fe_3O_4 (CLIO) MNS, respectively (Fig. 9) [38]. This increased MR contrast enhancement was tested to detect breast and ovarian cancer tumor in mice after Herceptin conjugation and intravenous injection (Fig. 9) [38]. $MnFe_2O_4$-Herceptin conjugates produced higher contrast than CLIO-Herceptin conjugates at the tumor site after 2 h (Fig. 9 a–d). Quantitatively, r_2 increase up to 34 % was observed for $MnFe_2O_4$-Herceptin conjugates in comparison to 5 and 13 % for CLIO-Herceptin conjugates and 12 nm Fe_3O_4-Herceptin conjugates, respectively (Fig. 9 e,f).

6.2 Nanoassembly of the MNS

Nanoassembly of MNS made up of numerous MNS have shown to increase r_2 relaxivity since an individual MNS in the nanoassembly is more efficient at dephasing the spins of the surrounding water protons [149]. For example, Feridex exhibits much higher r_2 relaxivity than monocrystalline iron oxide MNS because Feridex consists of several iron oxide nanoparticles embedded in a dextran shell [36]. Advances in chemical synthesis have enabled the preparation of nanoassemblies of tunable size and shape. Fe_3O_4 MNS have been assembled on dye-doped mesoporous silica nanoparticles (Fig. 10a) [37, 150]. The r_2 value of Fe_3O_4 coated silica nanoparticles was 2.8 times higher than that of well-dispersed Fe_3O_4 nano-particles (Fig. 10b) [150]. After subcutaneous injection into each dorsal shoulder of a nude mouse, MCF-7 cells labeled with Fe_3O_4-MNS were clearly detected as a dark volume of subcutaneous tumor in the T_2-weighted MR image, while the unlabeled MCF-7 cells did not show any MR contrast enhancement [150]. We have demonstrated controlled assembly of 6 nm amine functionalized Fe_3O_4 MNS [151]. The size of aggregates was ~40 nm and the

r_2 value was 315 mM^{-1} s^{-1}, which was significantly higher than r_2 of monodisperse 6 nm Fe_3O_4 (~100 mM^{-1} s^{-1}) [38].

6.3 Coating of MNS

Typically, the role of the MNS coating is to provide stability, biocompatibility, and enhanced blood circulation times. In addition, the coating on MNS affect the r_2 relaxivity since it can increase the residence time of the surrounding water molecules by forming hydrogen bonds [152]. For example, polyethylene glycol (PEG) is one of the most common coatings that is used to make MNS stable in aqueous/biological media. Each ethylene glycol subunit in the PEG associates with two or three water molecules which slows water diffusion, resulting in a high r_2 relaxivity [152].

We have developed MNS with Fe_3O_4 core and PEG coating that shows excellent buffer stability [83]. It was found that the PEG coating not only provides stability but the thickness of PEG coating also affects the r_2 relaxivity of Fe_3O_4 MNS. The thickness was varied by changing the molecular weight of PEG that resulted in different r_2 relaxivities. The r_2 relaxivity of 12 nm Fe_3O_4 MNS was found at 160, 194, 277, and 396 mM^{-1} s^{-1} when the molecular weight of PEG was 200, 400, 500, and 600 Da (Fig. 11). Bao et al. reported different r_2 relaxivities for phospholipid (DSPE)-PEG-coated Fe_3O_4 MNS by changing their core size (5 and 14 nm) and PEG length (mol. wt. 550, 750, 1000, 2000, and 5000). The highest r_2 value of 385 mM^{-1} s^{-1} was obtained for 14 nm Fe_3O_4 MNS coated with DSPE-PEG1000 [39]. In vivo tumor imaging was done using Fe_3O_4 MNS (5 and 14 nm) coated with DSPE-PEG1000 and conjugated with antibodies against mouse VEGFR-1. Tumors were induced by implanting human U87 glioblastoma cells subcutaneously in the nude mice. Tail vein injection of the 14 nm Fe_3O_4 MNS with r_2 relaxivity ~385 mM^{-1} s^{-1} produced more T_2 contrast enhancement of the tumor tissues in comparison to 5 nm Fe_3O_4 whose relaxivity was 130 mM^{-1} s^{-1}.

Silica coating on MNS is another common method to provide aqueous stability. It has been observed that r_2 relaxivity of MNS decreases with increment in silica shell thickness. Pinho et al. observed a systematic decrease in the r_2 relaxivity, from 228 to 23 mM^{-1} s^{-1}, after coating silica shell up to 20 nm on a 10 nm γ-Fe_2O_3 MNS [95]. The authors attributed this effect to two regions of silica shell coating, an inner water-impermeable layer and an outer water-permeable layer. The outer layer provided colloidal stability while the impermeable layer reduced the interaction between the MNS and water protons significantly, resulting in a drop in r_2 relaxivity.

6.4 MNS with Metal Core

Although MNS with ferrite cores are promising MRI contrast agents, their saturation magnetization can be further improved since a portion of their magnetic spins cancels each other. MNS with metallic core such as Fe, Co, FeCo, FePt, and CoPt exhibit higher saturation magnetization since all their magnetic spins align in one direction and there is no canceled spin. Saturation magnetization of bulk FeCo and Fe is 240 and 218 emu/g, respectively compared to 90 emu/g of bulk Fe_3O_4 MNS. However, each metallic MNS has a specific limitation as MRI contrast agents. For example, FePt and CoPt are chemically stable

but potentially toxic due to the possibility of leaching of Pt [153]. Fe, Co, and FeCo nanoparticles are biocompatible but are chemically unstable in air and prone to oxidation. To stabilize MNS with metallic core and maintain their magnetic properties, a number of coatings have been applied. MNS with Fe core and ferrite shell were reported that exhibited long-term stability in air [44–46]. Sun et al. reported bcc Fe/Fe_3O_4 core/shell MNS. Due to the high magnetization of Fe core, the r_2 relaxivity of Fe/Fe_3O_4 MNS (220 mM^{-1} s^{-1}) was found ~10 times higher than r_2 of Fe_3O_4 MNS (24 mM^{-1} s^{-1}) of the same size and coating [44, 56] and 2 times higher than the typical iron oxide NP contrast agent Feridex (110 mM^{-1} s^{-1}). However, no in vitro or in vivo studies were reported. Weissleder et al. further improved the r_2 relaxivity up to 430 mM^{-1} s^{-1} by coating $MnFe_2O_4$ shell on Fe nanoparticles. The authors intravenously injected $Fe/MnFe_2O_4$ MNS, Fe_3O_4 MNS of the same size and cross-linked iron oxide (CLIO). Taken at 3 h postinjection, the images verified that $Fe/MnFe_2O_4$ MNS resulted in the most significant darkening compared to CLIO and Fe_3O_4 MNS [46]. Dai et al. developed FeCo nanoparticles embedded in graphitic carbon (GC) shell that were discrete, chemically functionalized, and water soluble as desired for biological applications. Due to the high saturation magnetization, FeCo/GC MNS exhibited very high r_2 values (644 mM^{-1} s^{-1}). During in vivo intravascular MR imaging of the blood pool in the rabbit, mesenchymal stem cells labeled with FeCo/GC MNS showed significantly higher T_2 negative contrast enhancement compared to the ones labeled with Feridex [43, 52].

7 Thermally Activated MNS for Cancer Therapeutics

With the capability to generate thermal energy at targeted areas, MNS can be used in cancer therapeutics [5, 12, 154]. Compared with photodynamic therapy agents such as gold and graphene, MNS are advantageous for targets that reside deep inside the biological system without penetration depth problem. In addition, the fact that magnetic field causes no adverse effect on biological tissues serves as a distinctive benefit for noninvasive, in vivo applications.

The use of MNS in cancer therapeutic has been divided into three categories; (i) magnetic hyperthermia where MNS kill tumor cells via increase in tissue temperature; (ii) chemotherapy where MNS deliver a drug and trigger release at the tumor site; (iii) biotherapy where MNS are highly effective carrier platforms for bioactive molecules such as siRNA, oligos, and genes and facilitate transport of biomolecules in plasma membrane penetration necessary for cell internalization.

7.1 Magnetic Hyperthermia: MNS as Heat Generators

Targeted MNS can accumulate at the tumor site and increase the tissue temperature under an external RF field. Since the cancer tissues have higher heat sensitivity than normal tissues, thermal activation of MNS can be used to selectively kill tumor cells in the range of 41–47 °C [69]. As mentioned earlier, as MNS with high SAR have high efficacy for killing cancer cells, a variety of next-generation MNS with high SAR have been developed [155–157]. $(Zn_{0.4}Mn_{0.6})Fe_2O_4$ MNS have shown high SAR value of 432 W/g which is ~4 times higher than SAR of Feridex (115 W/g). The high SAR of $(Zn_{0.4}Mn_{0.6})Fe_2O_4$ MNS resulted in 84.4 % death of HeLa cancer cells in comparison to 13.5 % from Feridex (Fig. 12) [42].

Similarly, 82 % of Hela cells died when treated with $CoFe_2O_4$ MNS with SAR value of 238 W/g at 168 kHz [158]. Cheon et al. reported a significant increase in the SAR values of MNS by synthesizing core/shell MNS with hard ferromagnetic core and soft ferromagnetic shell [159]. Due to the exchange coupling between core and shell of MNS, the core/shell MNS showed SAR up to 3034 W/g which are an order of magnitude larger than SAR of conventional ferrite MNS (~300 W/g). Due to the high SAR values, the therapeutic efficacy of these MNS under RF was found superior to a common anticancer drug (doxorubicin). The same amounts (75 μg) of MNS and doxorubicin were injected into the tumor of a nude mice xenografted with cancer cells (U87MG). The tumor was clearly eliminated in 18 days in the group treated with the core/shell MNS, while in the doxorubicin-treated group tumor growth slowed initially, but then regrew after 18 days [159]. Recently, the same group reported Gd (III) texaphyrins (GdTx) conjugated $ZnFe_2O_4$ MNS with SAR of 471 W/g designed for hyperthermic treatment for apoptosis. This system is a double-effector MNS that generates heat as well as reactive oxygen species (ROS) which remarkably increased the degree of apoptotic cell death. Xenograft tumors in mice treated with the double-effector MNS were eliminated within 8 days whereas the tumor in untreated mice increased eightfold in 8 days [160].

7.2 Biotherapy: MNS as Carrier for Gene Therapeutics

Gene therapy is a technique that uses DNA and antisense RNA (siRNA) to treat and prevent disease via gene expression and gene silencing of defective genes [161, 162]. The coupling of nucleic acids with MNS improves the plasma pharmacokinetics and plasma membrane penetration of nucleic acids necessary for internalization into cells [162]. MNS designed for gene therapy have been coated with cationic polymers such as polyethylenimine (PEI), polyamidoamine, or chitosan in order to conjugate with negatively charged nucleic acids. While the cationic MNS have shown great success in vitro, their applicability in vivo has been limited because of toxicity and instability in biological media [163]. Zhang et al. coated MNS with a copolymer of PEI, PEG, and chitosan (NP-CP-PEI) [164]. The chitosan and PEG suppressed the PEI toxicity while PEG also provided the stability. NP-CP-PEI demonstrated an innocuous toxic profile and a high level of expression of the delivered plasmid DNA in a C6 xenograft mouse model, while MNS coated with only PEI or chitosan showed high toxicity or low gene transfection efficiency, respectively [164]. The attachment of the targeting ligand, chlorotoxin (CTX), to NP-CP-PEI enhanced the gene transfection efficiency. Histology analysis and confocal microscopy of the C6 xenograft tumor sections showed more cells expressing GFP in tumors treated with the NP-CP-PEI attached with CTX compared to NP-CP-PEI without CTX [165]. One alternative to the cationic coatings was offered by conjugating siRNA to MNS by covalent bonding. Medarova et al. developed a dual purpose probe for the simultaneous noninvasive imaging and delivery of siRNAs to tumors. This probe consisted of MNS labeled with Cy5.5 dye and conjugated to a synthetic siRNA duplex targeting a gene of interest. With use of model (green fluorescent protein, GFP) and therapeutic (surviving) genes, the authors demonstrated that the targeting and delivery of the probe could be monitored in vivo by MRI and optical imaging. In addition, they were able to follow the silencing process by optical imaging and to correlate it with histological data [86, 87].

7.3 Chemotherapy: MNS as Drug Carrier/Release Trigger for Chemotherapeutics

Chemotherapy focuses on the treatment of disease through delivery of small molecule drug formulations [88]. Most of the drugs do not have cell-targeting capabilities which results in undesirable side effects when internalized by healthy cells. The success of MNS in diagnostic imaging has generated considerable interest in their use as drug delivery vehicles. MNS coatings provide anchor points to which drug molecules can be coupled. Integrating the drugs into MNS improves their targeting abilities, limits their side effects, and allows increment of the drug dosage at the diseased tissue [5, 10]. Currently, several drugs have been combined with MNS for cancer chemotherapy, including paclitaxel (PTX), doxorubicin (DOX), and methotrexate (MTX) [89, 90]. The therapeutic moieties can be covalently bonded to MNS with cleavable linkages, encapsulated in the hydrophobic coating on MNS, or physically absorbed on the surface of MNS.

An ideal drug delivery vehicle should have efficient drug loading and controllable drug release. In applications where the drug (such as MTX) has an affinity for the target cell, it can be advantageous to graft the drug to the surface of the MNS. Kohler et al. demonstrated covalent attachment of MTX to the surface of a PEG-coated MNS via a cleavable amide linkage [89]. However, the drug loading capacity via direct conjugation was found low due to the small number of functional groups on the surface of MNS. Hollow MNS have been used to increase chemotherapeutic efficacy due to higher drug loading capacity [166]. Sun et al. utilized porous hollow Fe_3O_4 MNS with 5 times higher cisplatin loading compared to solid Fe_3O_4 MNS [167]. Once coupled with Herceptin to the surface, the cisplatin-loaded hollow NPs targeted breast cancer SK-BR-3 cells with IC_{50} reaching 2.9 μM, much lower than 6.8 μM needed for free cisplatin. Labheshwar et al. coated a PEO-PPO diblock copolymer (Pluronic F127) on oleic acid coated MNS, where a hydro-phobic region in the oleic acid/PPO layer provided drug loading of 8.2 and 9.5 % for DOX and PTX, respectively [168]. They found that MNS loaded with both DOX and PTX in a 1:1 ratio demonstrated highly synergistic antiproliferative activity in MCF-7 breast cancer cells relative to MNS loaded with only DOX or PTX.

The thermal energy from MNS has been used as an external trigger for controlled drug release. Thomas et al. loaded mesoporous silica nanoparticles with DOX and 15 nm $(Zn_{0.4}Fe_{0.6})Fe_2O_4$ MNS and capped the pores with cucurbit [6] uril that functioned as a heat labile molecular valve [169]. There was no drug release at the room temperature since the pores of the mesoporous silica remain capped, but under an external RF field, decapping occurred due to thermal activation of MNS, releasing most of the drug. In vitro, this controlled drug release killed 7-times more breast cancer cells. MNS coated with thermally responsive agents (e.g., hydrogels, thermosensitive polymers, lipids) have been explored where temperature works as a trigger for drug release [74, 170]. Recently, we reported poly(*N*-isopropylacrylamide) encapsulated Fe_3O_4 MNS in which DOX was loaded into the hydrogel via absorption. Drug release in presence of RF field was found 2 times higher than in absence of RF field due to thermal activation of MNS. In vitro localized drug delivery studies of the DOX loaded hydrogel-MNS composite with HeLa cell lines resulted in more than 80 % cell death under external RF field compared to 40 % cell death without RF field (Fig. 13) [83].

8 Summary and Outlook

Magnetic nanostructures (MNS) truly represent a prototypical nanotechnology platform in the sense that their properties and phenomena are unquestionably size dependent in the nanoscale regime. Nominal ferrimagnetic behavior of MNS changes to superparamagnetism below ~10–15 nm size scale, which is essential for colloidal stability of MNS. The perturbations of protons in vicinity of the MNS provide the essential characteristics for contrast in MRI, while enthalpic contributions from external RF field generate localized thermal energy for therapeutic purpose. Thus, the combined *theranostic* attributes of MNS arise from diagnostic imaging and thermal therapy combination.

Over and beyond the technical and scientific aspects of theranostic administration of cancer, MNS also embody the other important attribute of nanotechnology in terms of complementarity, integration, and synergy of nominally disparate fields and subjects. For just MNS alone, these subjects and technical themes include: physics of magnetism, chemistry of synthesis, materials science of structure–property relationship, surface science of functionalization, biomedical engineering in MR imaging protocols and RF activation parameters, and the core biology and medical themes of cancer targeting, diagnostics imaging, and therapy. As a result, this has brought together scientists, engineers, and clinical practitioners from diverse backgrounds for more than a decade to advance biomedical sensing, diagnostics, and therapeutics.

As demonstrated by the examples highlighted in this chapter, remarkable advances have been made in the recent decade to harness the size, composition, and size-dependent properties of MNS for cancer diagnostics, diagnostic imaging, and localized therapy. MNS continue to exhibit realistic potential to address diagnostic imaging by MRI and localized therapy via thermal activation and/or timed therapeutic cargo release. In particular, it has been shown that appropriate choice of composition, size, and surface functionalization has the potential for synergistic combination of diagnostics MR imaging and thermally activated therapy.

Despite some promising results obtained so far, including in vivo animal studies, there are specific challenges for effective use of MNS in humans; the final objective for any cancer theranostic platform. Regulatory approval for use in humans will require further and extensive safety and toxicology studies. The composition, surface properties, drug loading, biodistribution, and pharmacokinetics are the diverse factors that may affect the toxicity of the MNS in a direct or indirect manner and need to be understood thoroughly. Limitations also exist for targeting efficiency, the lack of homogeneous MNS penetration, and inadequate delivery of therapeutics into the tumor volume.

Research is continuing in this regard; including development of new magnetic core materials with higher relaxivity and thermal activation properties, along with design of new coating materials to improve the pharmacokinetics, biodistribution, and biocompatibility. Success with MRI and progress over the past few years offer considerable prospects for eventual diagnostic and therapeutic translation of MNS technology. Indeed, several diagnostic clinical trials using MNS have been initiated over the past few years. The increasing trend

toward in vivo studies in animals and subsequent escalation to clinical trials are expected to help translate MNS from the laboratory to the clinic.

References

1. Kim J, Piao Y, Hyeon T. Multifunctional nanostructured materials for multimodal imaging, and simultaneous imaging and therapy. Chem Soc Rev. 2009; 38(2):372–390. [PubMed: 19169455]
2. Sun C, Lee JSH, Zhang MQ. Magnetic nanoparticles in MR imaging and drug delivery. Adv Drug Deliv Rev. 2008; 60(11):1252–1265. [PubMed: 18558452]
3. Ho D, Sun XL, Sun SH. Monodisperse magnetic nanoparticles for theranostic applications. Acc Chem Res. 2011; 44(10):875–882. [PubMed: 21661754]
4. Yoo D, et al. Theranostic magnetic nanoparticles. Acc Chem Res. 2011; 44(10):863–874. [PubMed: 21823593]
5. Veiseh O, Gunn JW, Zhang MQ. Design and fabrication of magnetic nanoparticles for targeted drug delivery and imaging. Adv Drug Deliv Rev. 2010; 62(3):284–304. [PubMed: 19909778]
6. Xu CJ, Sun SH. New forms of superparamagnetic nanoparticles for biomedical applications. Adv Drug Deliv Rev. 2013; 65(5):732–743. [PubMed: 23123295]
7. Cole AJ, Yang VC, David AE. Cancer theranostics: the rise of targeted magnetic nanoparticles. Trends Biotechnol. 2011; 29(7):323–332. [PubMed: 21489647]
8. Livingston JD. A review of coercivity mechanisms. J Appl Phys. 1981; 52(3):2544–2548.
9. Reddy LH, et al. Magnetic nanoparticles: design and characterization, toxicity and biocompatibility. Pharmaceutical and biomedical applications. Chem Rev. 2012; 112(11):5818–5878. [PubMed: 23043508]
10. McCarthy JR, Weissleder R. Multifunctional magnetic nanoparticles for targeted imaging and therapy. Adv Drug Deliv Rev. 2008; 60(11):1241–1251. [PubMed: 18508157]
11. Misra RDK. Magnetic nanoparticle carrier for targeted drug delivery: perspective, outlook and design. Mater Sci Technol. 2008; 24(9):1011–1019.
12. Kievit FM, Zhang MQ. Surface engineering of iron oxide nanoparticies for targeted cancer therapy. Acc Chem Res. 2011; 44(10):853–862. [PubMed: 21528865]
13. Jun YW, Lee JH, Cheon J. Chemical design of nanoparticle probes for high-performance magnetic resonance imaging. Angew Chem Int Ed. 2008; 47(28):5122–5135.
14. Lee N, Hyeon T. Designed synthesis of uniformly sized iron oxide nanoparticles for efficient magnetic resonance imaging contrast agents. Chem Soc Rev. 2012; 41(7):2575–2589. [PubMed: 22138852]
15. De M, et al. Hybrid magnetic nanostructures (MNS) for magnetic resonance imaging applications. Adv Drug Deliv Rev. 2011; 63(14–15):1282–1299. [PubMed: 21851844]
16. Caravan P, et al. Gadolinium(III) chelates as MRI contrast agents: structure, dynamics, and applications. Chem Rev. 1999; 99(9):2293–2352. [PubMed: 11749483]
17. Caravan P. Strategies for increasing the sensitivity of gadolinium based MRI contrast agents. Chem Soc Rev. 2006; 35(6):512–523. [PubMed: 16729145]
18. Frullano L, Meade TJ. Multimodal MRI contrast agents. J Biol Inorg Chem. 2007; 12(7):939–949. [PubMed: 17659368]
19. Na HB, Hyeon T. Nanostructured T1 MRI contrast agents. J Mater Chem. 2009; 19(35):6267–6273.
20. Na HB, Song IC, Hyeon T. Inorganic nanoparticles for MRI contrast agents. Adv Mater. 2009; 21(21):2133–2148.
21. Hahn PF, et al. 1st clinical-trial of a new superparamagnetic iron-oxide for use as an oral gastrointestinal contrast agent in MR imaging. Radiology. 1990; 175(3):695–700. [PubMed: 2343116]
22. Reimer P, Balzer T. Ferucarbotran (Resovist): a new clinically approved RES-specific contrast agent for contrast-enhanced MRI of the liver: properties, clinical development, and applications. Eur Radiol. 2003; 13(6):1266–1276. [PubMed: 12764641]

23. Koenig SH, Kellar KE. Theory of $1/T_1$ and $1/T_2$ NMRD profiles of solutions of magnetic nanoparticles. Magn Reson Med. 1995; 34(2):227–233. [PubMed: 7476082]
24. Jordan A, et al. Magnetic fluid hyperthermia (MFH): cancer treatment with AC magnetic field induced excitation of biocompatible superparamagnetic nanoparticles. J Magn Magn Mater. 1999; 201:413–419.
25. Fortin JP, et al. Size-sorted anionic iron oxide nanomagnets as colloidal mediators for magnetic hyperthermia. J Am Chem Soc. 2007; 129(9):2628–2635. [PubMed: 17266310]
26. Hergt R, Dutz S. Magnetic particle hyperthermia-biophysical limitations of a visionary tumour therapy. J Magn Magn Mater. 2007; 311(1):187–192.
27. Jun YW, et al. Nanoscale size effect of magnetic nanocrystals and their utilization for cancer diagnosis via magnetic resonance imaging. J Am Chem Soc. 2005; 127(16):5732–5733. [PubMed: 15839639]
28. Laurent S, et al. Magnetic iron oxide nanoparticles: synthesis, stabilization, vectorization, physicochemical characterizations, and biological applications. Chem Rev. 2008; 108(6):2064–2110. [PubMed: 18543879]
29. Roca AG, et al. Progress in the preparation of magnetic nanoparticles for applications in biomedicine. J Phys D Appl Phys. 2009; 42(22):224002.
30. Massart R. Preparation of aqueous magnetic liquids in alkaline and acidic media. IEEE Trans Magn. 1981; 17(2):1247–1248.
31. Gupta AK, Gupta M. Synthesis and surface engineering of iron oxide nanoparticles for biomedical applications. Biomaterials. 2005; 26(18):3995–4021. [PubMed: 15626447]
32. Loo AL, et al. Synthesis of magnetic nanoparticles in bicontinuous microemulsions. Effect of surfactant concentration. J Mater Sci. 2008; 43(10):3649–3654.
33. Murray CB, Kagan CR, Bawendi MG. Synthesis and characterization of monodisperse nanocrystals and close-packed nanocrystal assemblies. Annu Rev Mater Sci. 2000; 30:545–610.
34. Park J, et al. Ultra-large-scale syntheses of monodisperse nanocrystals. Nat Mater. 2004; 3(12): 891–895. [PubMed: 15568032]
35. Wang YXJ, Hussain SM, Krestin GP. Superparamagnetic iron oxide contrast agents: physicochemical characteristics and applications in MR imaging. Eur Radiol. 2001; 11(11):2319–2331. [PubMed: 11702180]
36. Jung CW, Jacobs P. Physical and chemical-properties of superparamagnetic iron-oxide MR contrast agents—ferumoxides, ferumoxtran, ferumoxsil. Magn Reson Imaging. 1995; 13(5):661–674. [PubMed: 8569441]
37. Lee JH, et al. Dual-mode nanoparticle probes for high-performance magnetic resonance and fluorescence imaging of neuroblastoma. Angew Chem Int Ed. 2006; 45(48):8160–8162.
38. Lee JH, et al. Artificially engineered magnetic nanoparticles for ultra-sensitive molecular imaging. Nat Med. 2007; 13(1):95–99. [PubMed: 17187073]
39. Tong S, et al. Coating optimization of superparamagnetic iron oxide nanoparticles for high T-2 relaxivity. Nano Lett. 2010; 10(11):4607–4613. [PubMed: 20939602]
40. Lee N, et al. Magnetosome-like ferrimagnetic iron oxide nanocubes for highly sensitive MRI of single cells and transplanted pancreatic islets. Proc Natl Acad Sci USA. 2011; 108(7):2662–2667. [PubMed: 21282616]
41. Barcena C, et al. Zinc ferrite nanoparticles as MRI contrast agents. Chem Commun. 2008; 19:2224–2226.
42. Jang JT, et al. Critical enhancements of MRI contrast and hyperthermic effects by dopant-controlled magnetic nanoparticles. Angew Chem Int Ed. 2009; 48(7):1234–1238.
43. Seo WS, et al. FeCo/graphitic-shell nanocrystals as advanced magnetic-resonance-imaging and near-infrared agents. Nat Mater. 2006; 5(12):971–976. [PubMed: 17115025]
44. Lacroix LM, et al. Stable single-crystalline body centered cubic Fe nanoparticles. Nano Lett. 2011; 11(4):1641–1645. [PubMed: 21417366]
45. Lee H, Yoon TJ, Weissleder R. Ultrasensitive detection of bacteria using core-shell nanoparticles and an NMR-filter system. Angew Chem Int Ed. 2009; 48(31):5657–5660.

46. Yoon TJ, et al. Highly magnetic core-shell nanoparticles with a unique magnetization mechanism. Angew Chem Int Ed. 2011; 50(20):4663–4666.
47. Hu FQ, et al. High-performance nanostructured MR contrast probes. Nanoscale. 2010; 2(10):1884–1891. [PubMed: 20694208]
48. Hu FQ, et al. Highly dispersible, superparamagnetic magnetite nanoflowers for magnetic resonance imaging. Chem Commun. 2010; 46(1):73–75.
49. Morales MP, et al. Surface and internal spin canting in gamma-Fe2O3 nanoparticles. Chem Mater. 1999; 11(11):3058–3064.
50. Puntes VF, Krishnan KM, Alivisatos AP. Colloidal nanocrystal shape and size control: the case of cobalt. Science. 2001; 291(5511):2115–2117. [PubMed: 11251109]
51. Cordente N, et al. Synthesis and magnetic properties of nickel nanorods. Nano Lett. 2001; 1(10): 565–568.
52. Desvaux C, et al. Multimillimetre-large superlattices of air-stable iron-cobalt nanoparticles. Nat Mater. 2005; 4(10):750–753. [PubMed: 16155574]
53. Schutz-Sikma EA, et al. Probing the chemical stability of mixed ferrites: implications for magnetic resonance contrast agent design. Chem Mater. 2011; 23(10):2657–2664. [PubMed: 21603070]
54. Colombo M, et al. Biological applications of magnetic nanoparticles. Chem Soc Rev. 2012; 41(11):4306–4334. [PubMed: 22481569]
55. Bao YP, Krishnan KM. Preparation of functionalized and gold-coated cobalt nanocrystals for biomedical applications. J Magn Magn Mater. 2005; 293(1):15–19.
56. Peng S, et al. Synthesis and stabilization of monodisperse Fe nanoparticles. J Am Chem Soc. 2006; 128(33):10676–10677. [PubMed: 16910651]
57. Ni XM, et al. Silica-coated iron nanoparticles: shape-controlled synthesis, magnetism and microwave absorption properties. Mater Chem Phys. 2010; 120(1):206–212.
58. Cozzoli PD, Pellegrino T, Manna L. Synthesis, properties and perspectives of hybrid nanocrystal structures. Chem Soc Rev. 2006; 35(11):1195–1208. [PubMed: 17057845]
59. Donega CD. Synthesis and properties of colloidal heteronanocrystals. Chem Soc Rev. 2011; 40(3): 1512–1546. [PubMed: 20972490]
60. Gao JH, Gu HW, Xu B. Multifunctional magnetic nanoparticles: design, synthesis, and biomedical applications. Acc Chem Res. 2009; 42(8):1097–1107. [PubMed: 19476332]
61. Xu CJ, Wang BD, Sun SH. Dumbbell-like Au-Fe_3O_4 nanoparticles for target-specific platin delivery. J Am Chem Soc. 2009; 131(12):4216–4217. [PubMed: 19275156]
62. Gu HW, et al. Facile one-pot synthesis of bifunctional heterodimers of nanoparticles: a conjugate of quantum dot and magnetic nanoparticles. J Am Chem Soc. 2004; 126(18):5664–5665. [PubMed: 15125648]
63. Kwon KW, Shim M. gamma-Fe_2O_3/II–VI sulfide nanocrystal heterojunctions. J Am Chem Soc. 2005; 127(29):10269–10275. [PubMed: 16028938]
64. Choi JH, et al. Multimodal biomedical imaging with asymmetric single-walled carbon nanotube/iron oxide nanoparticle complexes. Nano Lett. 2007; 7(4):861–867. [PubMed: 17335265]
65. Gao JH, et al. Fluorescent magnetic nanocrystals by sequential addition of reagents in a one-pot reaction: a simple preparation for multifunctional nanostructures. J Am Chem Soc. 2007; 129(39): 11928–11935. [PubMed: 17824703]
66. Pittet MJ, et al. Labeling of immune cells for in vivo imaging using magnetofluorescent nanoparticles. Nat Protoc. 2006; 1(1):73–79. [PubMed: 17406214]
67. Wang DS, et al. Superparamagnetic Fe_2O_3 Beads-CdSe/ZnS quantum dots core-shell nanocomposite particles for cell separation. Nano Lett. 2004; 4(3):409–413.
68. Choi JS, et al. Self-confirming “AND” logic nanoparticles for fault-free MRI. J Am Chem Soc. 2010; 132(32):11015–11017. [PubMed: 20698661]
69. Gupta AK, et al. Recent advances on surface engineering of magnetic iron oxide nanoparticles and their biomedical applications. Nanomedicine. 2007; 2(1):23–39. [PubMed: 17716188]
70. Kohler N, Fryxell GE, Zhang MQ. A bifunctional poly(ethylene glycol) silane immobilized on metallic oxide-based nanoparticles for conjugation with cell targeting agents. J Am Chem Soc. 2004; 126(23):7206–7211. [PubMed: 15186157]

71. Xie J, et al. Controlled PEGylation of monodisperse Fe_3O_4 nanoparticles for reduced non-specific uptake by macrophage cells. Adv Mater. 2007; 19(20):3163–3166.
72. Mornet S, Portier J, Duguet E. A method for synthesis and functionalization of ultrasmall superparamagnetic covalent carriers based on maghemite and dextran. J Magn Magn Mater. 2005; 293(1):127–134.
73. Kim DH, et al. Targeting to carcinoma cells with chitosan- and starch-coated magnetic nanoparticles for magnetic hyperthermia. J Biomed Mater Res Part A. 2009; 88A(1):1–11.
74. Pradhan P, et al. Targeted temperature sensitive magnetic liposomes for thermochemotherapy. J Controlled Release. 2010; 142(1):108–121.
75. Wang LY, et al. Core@shell nanomaterials: gold-coated magnetic oxide nanoparticles. J Mater Chem. 2008; 18(23):2629–2635.
76. Ma DL, et al. Superparamagnetic Fe(x)Oy@SiO_2 core-shell nanostructures: controlled synthesis and magnetic characterization. J Phys Chem C. 2007; 111(5):1999–2007.
77. Fuertges F, Abuchowski A. The clinical efficacy of poly(ethylene glycol)-modified proteins. J Controlled Release. 1990; 11(1–3):139–148.
78. Harris JM, Chess RB. Effect of pegylation on pharmaceuticals. Nat Rev Drug Discov. 2003; 2(3): 214–221. [PubMed: 12612647]
79. Lutz JF, et al. One-pot synthesis of PEGylated ultrasmall iron-oxide nanoparticles and their in vivo evaluation as magnetic resonance imaging contrast agents. Biomacromolecules. 2006; 7(11):3132–3138. [PubMed: 17096542]
80. Kim SW, et al. Phosphine oxide polymer for water-soluble nanoparticles. J Am Chem Soc. 2005; 127(13):4556–4557. [PubMed: 15796504]
81. Xu CJ, et al. Dopamine as a robust anchor to immobilize functional molecules on the iron oxide shell of magnetic nanoparticles. J Am Chem Soc. 2004; 126(32):9938–9939. [PubMed: 15303865]
82. Amstad E, et al. Ultrastable iron oxide nanoparticle colloidal suspensions using dispersants with catechol-derived anchor groups. Nano Lett. 2009; 9(12):4042–4048. [PubMed: 19835370]
83. Jaiswal MK, et al. Thermoresponsive magnetic hydrogels as theranostic nanoconstructs. ACS Appl Mater Interfaces. 2014; 6(9):6237–6247. [PubMed: 24716547]
84. Molday RS, Mackenzie D. Immunospecific ferromagnetic iron-dextran reagents for the labeling and magnetic separation of cells. J Immunol Methods. 1982; 52(3):353–367. [PubMed: 7130710]
85. Weissleder R, Pittet MJ. Imaging in the era of molecular oncology. Nature. 2008; 452(7187):580–589. [PubMed: 18385732]
86. Medarova Z, et al. In vivo imaging of siRNA delivery and silencing in tumors. Nat Med. 2007; 13(3):372–377. [PubMed: 17322898]
87. Kumar M, et al. Image-guided breast tumor therapy using a small interfering RNA nanodrug. Cancer Res. 2010; 70(19):7553–7561. [PubMed: 20702603]
88. DeVita VT, Chu E. A history of cancer chemotherapy. Cancer Res. 2008; 68(21):8643–8653. [PubMed: 18974103]
89. Kohler N, et al. Methotrexate-immobilized poly(ethylene glycol) magnetic nanoparticles for MR imaging and drug delivery. Small. 2006; 2(6):785–792. [PubMed: 17193123]
90. Sun C, et al. In vivo MRI detection of gliomas by chlorotoxin-conjugated superparamagnetic nanoprobes. Small. 2008; 4(3):372–379. [PubMed: 18232053]
91. Bautista MC, et al. Surface characterisation of dextran-coated iron oxide nanoparticles prepared by laser pyrolysis and coprecipitation. J Magn Magn Mater. 2005; 293(1):20–27.
92. Wunderbaldinger P, Josephson L, Weissleder R. Crosslinked iron oxides (CLIO): a new platform for the development of targeted MR contrast agents. Acad Radiol. 2002; 9:S304–S306. [PubMed: 12188255]
93. Li W, et al. First-pass contrast-enhanced magnetic resonance angiography in humans using ferumoxytol, a novel ultrasmall superparamagnetic iron oxide (USPIO)-based blood pool agent. J Magn Reson Imaging. 2005; 21(1):46–52. [PubMed: 15611942]
94. Lu Y, et al. Modifying the surface properties of superparamagnetic iron oxide nanoparticles through a sol-gel approach. Nano Lett. 2002; 2(3):183–186.

95. Pinho SLC, et al. Fine tuning of the relaxometry of gamma-Fe_2O_3@SiO_2 nanoparticles by tweaking the silica coating thickness. ACS Nano. 2010; 4(9):5339–5349. [PubMed: 20795638]

96. Liong M, et al. Multifunctional inorganic nanoparticles for imaging, targeting, and drug delivery. ACS Nano. 2008; 2(5):889–896. [PubMed: 19206485]

97. Aslam M, Li S, Dravid VP. Controlled synthesis and stability of Co@SiO_2 aqueous colloids. J Am Ceram Soc. 2007; 90(3):950–956.

98. Yoo JW, Chambers E, Mitragotri S. Factors that control the circulation time of nanoparticles in blood: challenges, solutions and future prospects. Curr Pharm Des. 2010; 16(21):2298–2307. [PubMed: 20618151]

99. Chouly C, et al. Development of superparamagnetic nanoparticles for MRI: effect of particle size, charge and surface nature on biodistribution. J Microencapsul. 1996; 13(3):245–255. [PubMed: 8860681]

100. Gupta AK, Wells S. Surface-modified superparamagnetic nanoparticles for drug delivery: preparation, characterization, and cytotoxicity studies. IEEE Trans Nanobiosci. 2004; 3(1):66–73.

101. Decuzzi P, et al. The effective dispersion of nanovectors within the tumor microvasculature. Ann Biomed Eng. 2006; 34(4):633–641. [PubMed: 16568349]

102. Chertok B, David AE, Yang VC. Polyethyleneimine-modified iron oxide nanoparticles for brain tumor drug delivery using magnetic targeting and intra-carotid administration. Biomaterials. 2010; 31(24):6317–6324. [PubMed: 20494439]

103. Sun CR, et al. PEG-mediated synthesis of highly dispersive multifunctional superparamagnetic nanoparticles: their physicochemical properties and function in vivo. ACS Nano. 2010; 4(4): 2402–2410. [PubMed: 20232826]

104. Larsen EKU, et al. Size-dependent accumulation of PEGylated silane-coated magnetic iron oxide nanoparticles in murine tumors. ACS Nano. 2009; 3(7):1947–1951. [PubMed: 19572620]

105. Yallapu MM, et al. PEG-functionalized magnetic nanoparticles for drug delivery and magnetic resonance imaging applications. Pharm Res. 2010; 27(11):2283–2295. [PubMed: 20845067]

106. Longmire M, Choyke PL, Kobayashi H. Clearance properties of nano-sized particles and molecules as imaging agents: considerations and caveats. Nanomedicine. 2008; 3(5):703–717. [PubMed: 18817471]

107. Gratton SEA, et al. The effect of particle design on cellular internalization pathways. Proc Natl Acad Sci USA. 2008; 105(33):11613–11618. [PubMed: 18697944]

108. Moghimi SM. Exploiting bone-marrow microvascular structure for drug-delivery and future therapies. Adv Drug Deliv Rev. 1995; 17(1):61–73.

109. Moghimi SM. Mechanisms of splenic clearance of blood-cells and particles—towards development of new splenotropic agents. Adv Drug Deliv Rev. 1995; 17(1):103–115.

110. Villanueva A, et al. The influence of surface functionalization on the enhanced internalization of magnetic nanoparticles in cancer cells. Nanotechnology. 2009; 20(11):115103. [PubMed: 19420433]

111. Maeda H, et al. Tumor vascular permeability and the EPR effect in macromolecular therapeutics: a review. J Controlled Release. 2000; 65(1–2):271–284.

112. Jain RK. Transport of molecules, particles, and cells in solid tumors. Annu Rev Biomed Eng. 1999; 1:241–263. [PubMed: 11701489]

113. Fang J, Nakamura H, Maeda H. The EPR effect: unique features of tumor blood vessels for drug delivery, factors involved, and limitations and augmentation of the effect. Adv Drug Deliv Rev. 2011; 63(3):136–151. [PubMed: 20441782]

114. Prabhakar U, et al. Challenges and key considerations of the enhanced permeability and retention effect for nanomedicine drug delivery in oncology. Cancer Res. 2013; 73(8):2412–2417. [PubMed: 23423979]

115. Zhang Y, Kohler N, Zhang MQ. Surface modification of superparamagnetic magnetite nanoparticles and their intracellular uptake. Biomaterials. 2002; 23(7):1553–1561. [PubMed: 11922461]

116. Sinha R, et al. Nanotechnology in cancer therapeutics: bioconjugated nanoparticles for drug delivery. Mol Cancer Ther. 2006; 5(8):1909–1917. [PubMed: 16928810]

117. Kohler N, et al. Methotrexate-modified superparamagnetic nanoparticles and their intracellular uptake into human cancer cells. Langmuir. 2005; 21(19):8858–8864. [PubMed: 16142971]
118. Sun C, Sze R, Zhang MQ. Folic acid-PEG conjugated superparamagnetic nanoparticles for targeted cellular uptake and detection by MRI. J Biomed Mater Res Part A. 2006; 78A(3):550–557.
119. Montet X, Weissleder R, Josephson L. Imaging pancreatic cancer with a peptide-nanoparticle conjugate targeted to normal pancreas. Bioconjug Chem. 2006; 17(4):905–911. [PubMed: 16848396]
120. Gunn J, et al. A multimodal targeting nanoparticle for selectively labeling T cells. Small. 2008; 4(6):712–715. [PubMed: 18528851]
121. Hong S, et al. The binding avidity of a nanoparticle-based multivalent targeted drug delivery platform. Chem Biol. 2007; 14(1):107–115. [PubMed: 17254956]
122. Chertok B, et al. Glioma selectivity of magnetically targeted nanoparticles: a role of abnormal tumor hydrodynamics. J Controlled Release. 2007; 122(3):315–323.
123. Dobson J. Magnetic nanoparticles for drug delivery. Drug Dev Res. 2006; 67(1):55–60.
124. Wilson MW, et al. Hepatocellular carcinoma: regional therapy with a magnetic targeted carrier bound to doxorubicin in a dual MR imaging/conventional angiography suite—initial experience with four patients. Radiology. 2004; 230(1):287–293. [PubMed: 14695402]
125. Bulte JWM, Kraitchman DL. Iron oxide MR contrast agents for molecular and cellular imaging. NMR Biomed. 2004; 17(7):484–499. [PubMed: 15526347]
126. Artemov D, et al. MR molecular imaging of the Her-2/neu receptor in breast cancer cells using targeted iron oxide nanoparticles. Magn Reson Med. 2003; 49(3):403–408. [PubMed: 12594741]
127. Hu FQ, et al. Preparation of biocompatible magnetite nanocrystals for in vivo magnetic resonance detection of cancer. Adv Mater. 2006; 18(19):2553–2556.
128. Xie J, et al. Ultrasmall c(RGDyK)-coated Fe(3)O(4) nanoparticles and their specific targeting to integrin alpha(v)beta(3)-rich tumor cells. J Am Chem Soc. 2008; 130(24):7542. [PubMed: 18500805]
129. Bulte JWM, et al. Magnetodendrimers allow endosomal magnetic labeling and in vivo tracking of stem cells. Nat Biotechnol. 2001; 19(12):1141–1147. [PubMed: 11731783]
130. Frank JA, et al. Clinically applicable labeling of mammalian and stem cells by combining; superparamagnetic iron oxides and transfection agents. Radiology. 2003; 228(2):480–487. [PubMed: 12819345]
131. Bulte JWM. In vivo MRI cell tracking: clinical studies. Am J Roentgenol. 2009; 193(2):314–325. [PubMed: 19620426]
132. Berman SMC, Walczak P, Bulte JWM. Tracking stem cells using magnetic nanoparticles. Wiley Interdisc Rev Nanomed Nanobiotechnol. 2011; 3(4):343–355.
133. Ahrens ET, Bulte JWM. Tracking immune cells in vivo using magnetic resonance imaging. Nat Rev Immunol. 2013; 13(10):755–763. [PubMed: 24013185]
134. Srivastava AK, Bulte JWM. Seeing stem cells at work in vivo. Stem Cell Rev Rep. 2014; 10(1): 127–144.
135. Kircher MF, et al. In vivo high resolution three-dimensional imaging of antigenspecific cytotoxic T-lymphocyte trafficking to tumors. Cancer Res. 2003; 63(20):6838–6846. [PubMed: 14583481]
136. Daldrup-Link HE, et al. In vivo tracking of genetically engineered, anti-HER2/neu directed natural killer cells to HER2/neu positive mammary tumors with magnetic resonance imaging. Eur Radiol. 2005; 15(1):4–13. [PubMed: 15616814]
137. Anderson SA, et al. Magnetic resonance imaging of labeled T-Cells in a mouse model of multiple sclerosis. Ann Neurol. 2004; 55(5):654–659. [PubMed: 15122705]
138. Berman SMC, et al. Cell motility of neural stem cells is reduced after SPIO-labeling, which is mitigated after exocytosis. Magn Reson Med. 2013; 69(1):255–262. [PubMed: 22374813]
139. de Vries IJM, et al. Magnetic resonance tracking of dendritic cells in melanoma patients for monitoring of cellular therapy. Nat Biotechnol. 2005; 23(11):1407–1413. [PubMed: 16258544]
140. Verdijk P, et al. Sensitivity of magnetic resonance imaging of dendritic cells for in vivo tracking of cellular cancer vaccines. Int J Cancer. 2007; 120(5):978–984. [PubMed: 17163419]

141. Verdijk P, et al. Limited amounts of dendritic cells migrate into the T-Cell area of lymph nodes but have high immune activating potential in melanoma patients. Clin Cancer Res. 2009; 15(7): 2531–2540. [PubMed: 19318472]
142. Schuurhuis DH, et al. In situ expression of tumor antigens by messenger RNA-electroporated dendritic cells in lymph nodes of melanoma patients. Cancer Res. 2009; 69(7):2927–2934. [PubMed: 19318559]
143. Cruz LJ, et al. multimodal imaging of nanovaccine carriers targeted to human dendritic cells. Mol Pharm. 2011; 8(2):520–531. [PubMed: 21381651]
144. Janowski M, et al. Long-term MRI cell tracking after intraventricular delivery in a patient with global cerebral ischemia and prospects for magnetic navigation of stem cells within the CSF. PLoS ONE. 2014; 9(6):e97631. [PubMed: 24919061]
145. Moghimi SM, Hunter AC, Murray JC. Long-circulating and target-specific nanoparticles: theory to practice. Pharmacol Rev. 2001; 53(2):283–318. [PubMed: 11356986]
146. Huang J, et al. Effects of nanoparticle size on cellular uptake and liver MRI with polyvinylpyrrolidone-coated iron oxide nanoparticles. ACS Nano. 2010; 4(12):7151–7160. [PubMed: 21043459]
147. Joshi HM, et al. Effects of shape and size of cobalt ferrite nanostructures on their MRI contrast and thermal activation. J Phys Chem C. 2009; 113(41):17761–17767.
148. Zhao ZH, et al. Octapod iron oxide nanoparticles as high-performance T-2 contrast agents for magnetic resonance imaging. Nat Commun. 2013; 4:2266. [PubMed: 23903002]
149. Berret JF, et al. Controlled clustering of superparamagnetic nanoparticles using block copolymers: design of new contrast agents for magnetic resonance imaging. J Am Chem Soc. 2006; 128(5):1755–1761. [PubMed: 16448152]
150. Lee JE, et al. Uniform mesoporous dye-doped silica nanoparticles decorated with multiple magnetite nanocrystals for simultaneous enhanced magnetic resonance imaging, fluorescence imaging, and drug delivery. J Am Chem Soc. 2010; 132(2):552–557. [PubMed: 20017538]
151. Barick KC, et al. Nanoscale assembly of amine-functionalized colloidal iron oxide. J Magn Magn Mater. 2009; 321(10):1529–1532. [PubMed: 20160860]
152. LaConte LEW, et al. Coating thickness of magnetic iron oxide nanoparticles affects R-2 relaxivity. J Magn Reson Imaging. 2007; 26(6):1634–1641. [PubMed: 17968941]
153. Gao JH, et al. Multifunctional yolk-shell nanoparticles: a potential MRI contrast and anticancer agent. J Am Chem Soc. 2008; 130(35):11828–11833. [PubMed: 18681432]
154. Mahmoudi M, et al. Superparamagnetic iron oxide nanoparticles (SPIONs): development, surface modification and applications in chemotherapy. Adv Drug Deliv Rev. 2011; 63(1–2):24–46. [PubMed: 20685224]
155. Pollert E, et al. Search of new core materials for magnetic fluid hyperthermia: preliminary chemical and physical issues. Prog Solid State Chem. 2009; 37(1):1–14.
156. Lacroix LM, et al. Magnetic hyperthermia in single-domain monodisperse FeCo nanoparticles: evidences for Stoner-Wohlfarth behavior and large losses. J Appl Phys. 2009; 105(2):023911.
157. Mehdaoui B, et al. Large specific absorption rates in the magnetic hyperthermia properties of metallic iron nanocubes. J Magn Magn Mater. 2010; 322(19):L49–L52.
158. Franchini MC, et al. Bovine serum albumin-based magnetic nanocarrier for MRI diagnosis and hyperthermic therapy: a potential theranostic approach against cancer. Small. 2010; 6(3):366–370. [PubMed: 20020469]
159. Lee J-H, et al. Exchange-coupled magnetic nanoparticles for efficient heat induction. Nat Nano. 2011; 6(7):418–422.
160. Yoo D, et al. Double-effector nanoparticles: a synergistic approach to apoptotic hyperthermia. Angew Chem Int Ed. 2012; 51(50):12482–12485.
161. Mykhaylyk O, et al. siRNA delivery by magnetofection. Curr Opin Mol Ther. 2008; 10(5):493–505. [PubMed: 18830925]
162. McBain SC, et al. Magnetic nanoparticles as gene delivery agents: enhanced transfection in the presence of oscillating magnet arrays. Nanotechnology. 2008; 19(40):405102. [PubMed: 21832609]

163. Petri-Fink A, et al. Effect of cell media on polymer coated superparamagnetic iron oxide nanoparticles (SPIONs): colloidal stability, cytotoxicity, and cellular uptake studies. Eur J Pharm Biopharm. 2008; 68(1):129–137. [PubMed: 17881203]

164. Kievit FM, et al. PEI-PEG-Chitosan-copolymer-coated iron oxide nanoparticles for safe gene delivery: synthesis, complexation, and transfection. Adv Funct Mater. 2009; 19(14):2244–2251. [PubMed: 20160995]

165. Kievit FM, et al. Chlorotoxin labeled magnetic nanovectors for targeted gene delivery to glioma. ACS Nano. 2010; 4(8):4587–4594. [PubMed: 20731441]

166. Shin JM, et al. Hollow manganese oxide nanoparticles as multifunctional agents for magnetic resonance imaging and drug delivery. Angew Chem Int Ed. 2009; 48(2):321–324.

167. Cheng K, et al. Porous hollow Fe_3O_4 nanoparticles for targeted delivery and controlled release of cisplatin. J Am Chem Soc. 2009; 131(30):10637–10644. [PubMed: 19722635]

168. Jain TK, et al. Magnetic nanoparticles with dual functional properties: drug delivery and magnetic resonance imaging. Biomaterials. 2008; 29(29):4012–4021. [PubMed: 18649936]

169. Thomas CR, et al. Noninvasive remote-controlled release of drug molecules in vitro using magnetic actuation of mechanized nanoparticles. J Am Chem Soc. 2010; 132(31):10623–10625. [PubMed: 20681678]

170. Purushotham S, Ramanujan RV. Thermoresponsive magnetic composite nanomaterials for multimodal cancer therapy. Acta Biomater. 2010; 6(2):502–510. [PubMed: 19596094]

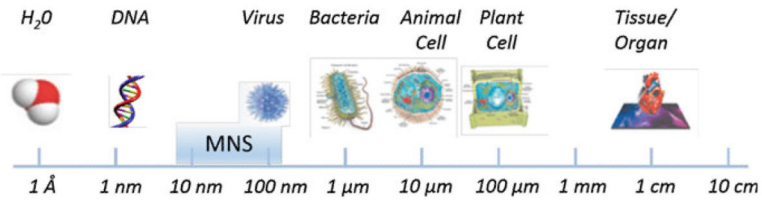

Fig. 1.

Size scale of MNS as compared to biomolecules. MNS can be adapted to include biomolecules, drugs, or targeting and imaging molecules to form targeted MNS theranostic agents

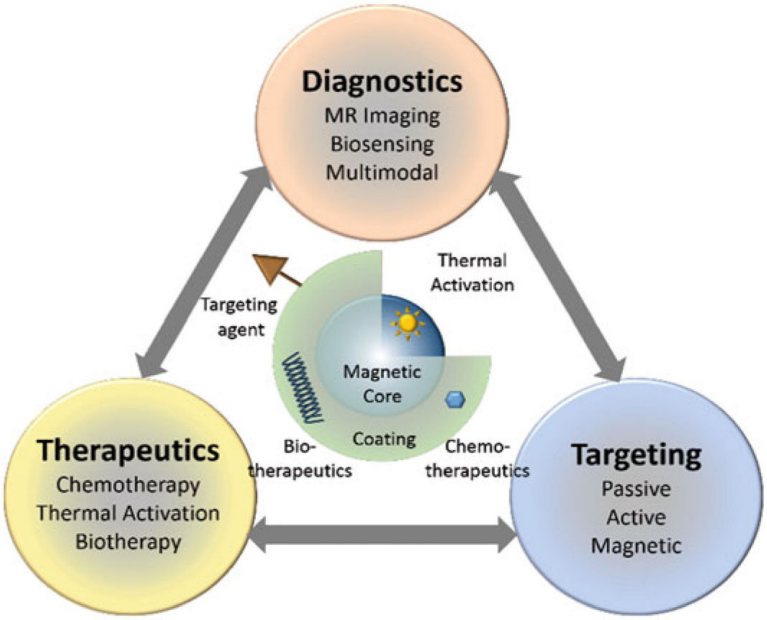

Fig. 2.

Functional architecture of MNS and theranostic modalities. MNS are comprised of thermally active magnetic core and biocompatible coating and/or functionalization that allows integration of targeting agents and bio/chemotherapeutics

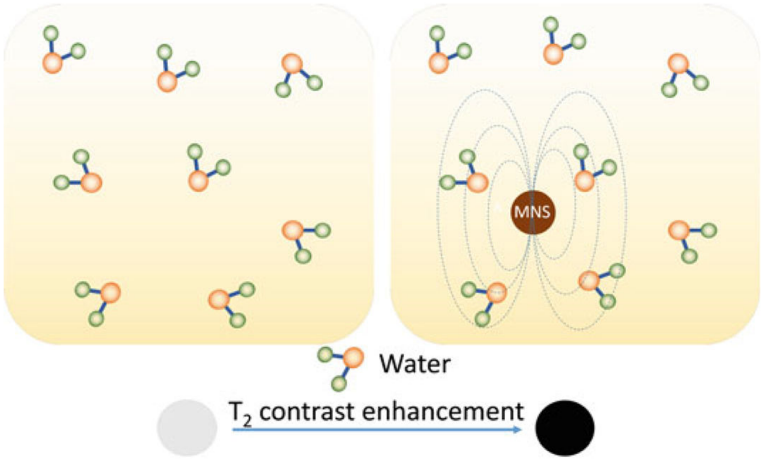

Fig. 3.

T_2 contrast enhancement in water due to MNS. When water molecules diffuse into the periphery of the induced dipole moment by MNS, the T_2 relaxation time of the water protons is shortened which enhances the negative contrast

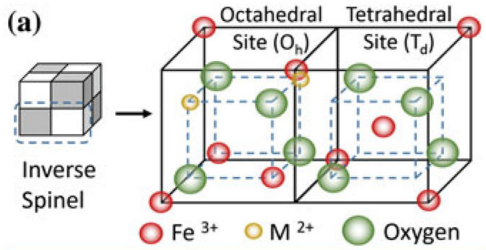

(c)	$MnFe_2O_4$	Fe_3O_4	$CoFe_2O_4$	$NiFe_2O_4$
Magnetic Moment	5 μ_B	4 μ_B	3 μ_B	2 μ_B
Saturation Magnetization (emu/g)	110	101	99	85
Relaxivity ($mM^{-1}s^{-1}$)	358	218	172	152

Fig. 4.

MFe_2O_4 (where *M* = Mn, Fe, Co, Ni) MNS with inverse spinel structure and its magnetic spin alignments. The mass magnetization values and r_2 relaxivity values of MFe_2O_4 MNS are proportional to the magnetic moments of the divalent ions (M^{2+}) [38]

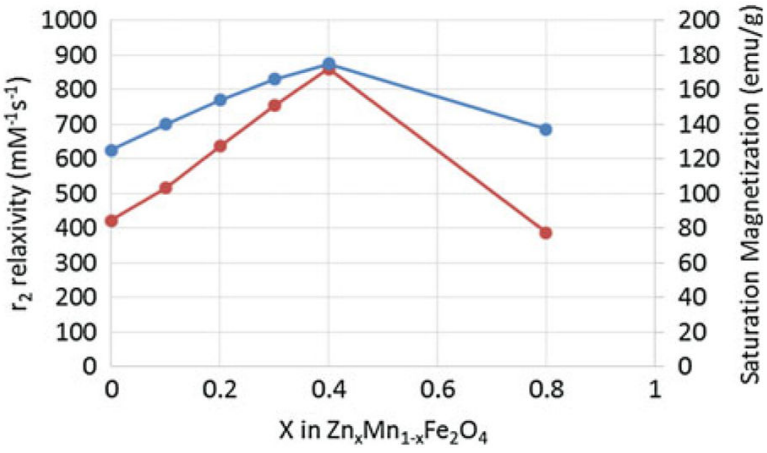

Fig. 5.

Saturation magnetization and r_2 relaxivity (at 4.5 T) of $(Zn_xMn_{1-x})Fe_2O_4$ MNS at different Zn^{2+} doping levels. The $(Zn_xMn_{1-x})Fe_2O_4$ MNS showed significantly high r_2 relaxivities compared to conventional iron oxide MNS [42]

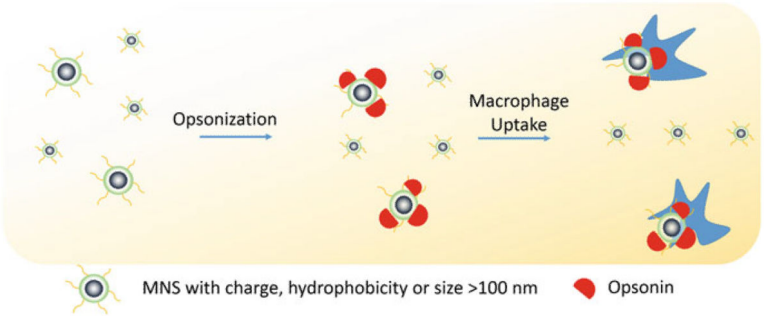

Fig. 6.

Schematic illustration of RES clearance of MNS. MNS larger than 100 nm are absorbed by circulating opsonin proteins that are recognized by macrophages and removed from the bloodstream

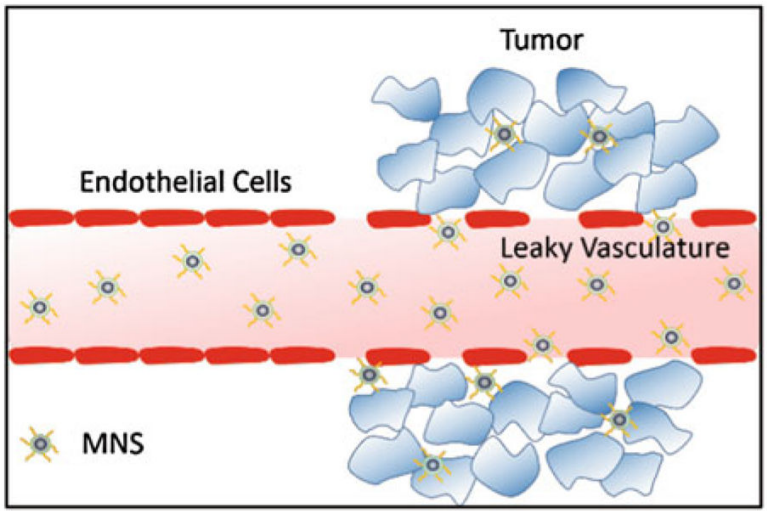

Fig. 7.

Passive targeting of MNS via enhanced permeability and retention (EPR) effect. The compromised vasculature of a solid tumor facilitates extravasation of MNS of size less than 200 nm from the circulation into the tumor interstitium, while endothelial cells are closely packed and present a barrier for MNS penetration

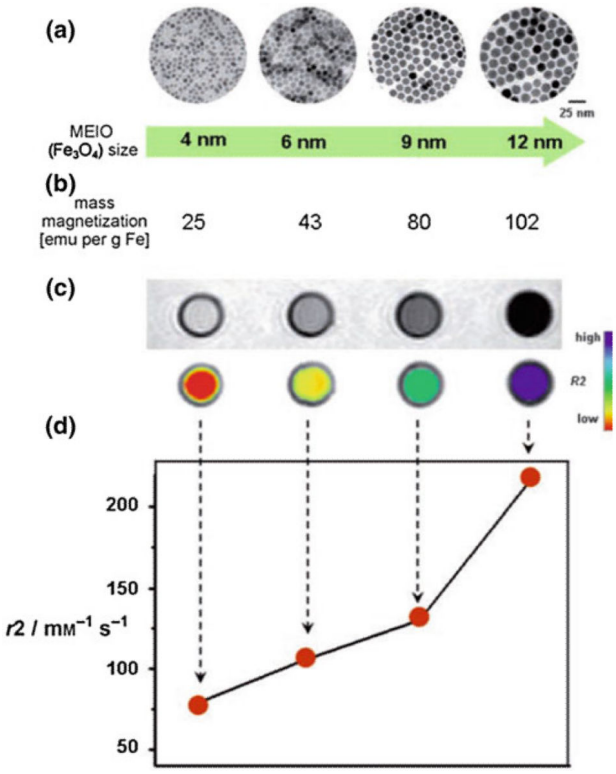

Fig. 8.

Size effects of Fe_3O_4 MNS on r_2 relaxivity. **a** TEM images, **b** saturation magnetization values, **c** T_2-weighted MR images (*top black* and *white*, *bottom* color), and **d** the r_2 relaxivity values of 4, 6, 9, and 12 nm sized Fe_3O_4 MNS. The r_2 relaxivity value increased with size of Fe_3O_4 MNS which resulted in the T_2 contrast change from *light gray* to *black* in T_2 weighted MR images or from *red* to *blue* in the corresponding color-coded images. Reprinted with permission from [27]. Copyright 2005 American Chemical Society

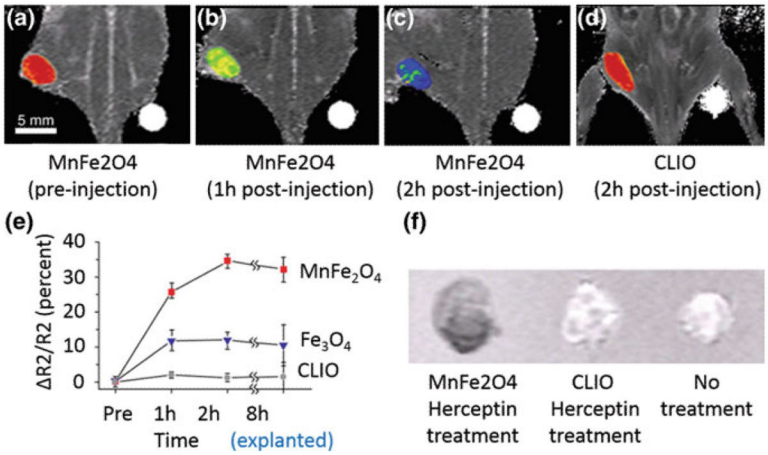

Fig. 9.

In vivo MR detection of cancer in a mouse implanted with the cancer cell line NIH3T6.7 using 12 nm $MnFe_2O_4$, 12 nm Fe_3O_4 and dextran coated cross-linked 4 nm Fe_3O_4 (CLIO) MNS. T_2-weighted MR images of the mouse (**a**) before injection, (**b**) after 1 h injection, and (**c**) after 2 h injection of $MnFe_2O_4$ in comparison to (**d**) after 2 h injection of CLIO. $MnFe_2O_4$-Herceptin conjugates produced higher contrast than CLIO-Herceptin conjugates at the tumor site after 2 h. **e** Plot of R_2 change versus time. Increase in R_2 up to 34 % was observed for $MnFe_2O_4$-Herceptin conjugates in comparison to 5 and 13 % for CLIO-Herceptin conjugate (*dots*) and 12 nm Fe_3O_4-Herceptin conjugates, respectively. **f** Change in R_2 values was confirmed in the ex vivo MR images of explanted tumors (8 h). Reprinted with permission from [38]. Copyright 2007 Nature Publishing Group

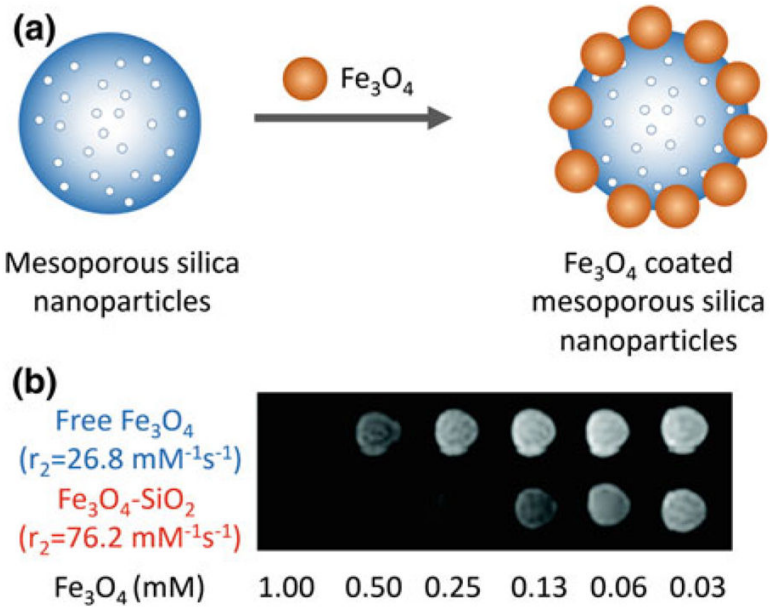

Fig. 10.

MR signal enhancement by assembly of Fe_3O_4 on SiO_2 nanoparticles. **a** Schematic illustration of the synthetic procedure for Fe_3O_4 decorated mesoporous silica nanoparticles. **b** Relaxivity values and T_2 weighted MR image of Fe_3O_4 decorated SiO_2 nanoparticles (Fe_3O_4-MSN) and free Fe_3O_4 nanoparticles. The r_2 relaxivity of Fe_3O_4 decorated SiO_2 nanoparticles was increased by 2.8 times as compared to free Fe_3O_4 nanoparticles, hence darker signal was observed in $\mathbf{T}_2$ weighted MR image at the same concentration of Fe. Reprinted with permission from Ref. [150]. Copyright 2010 American Chemical Society

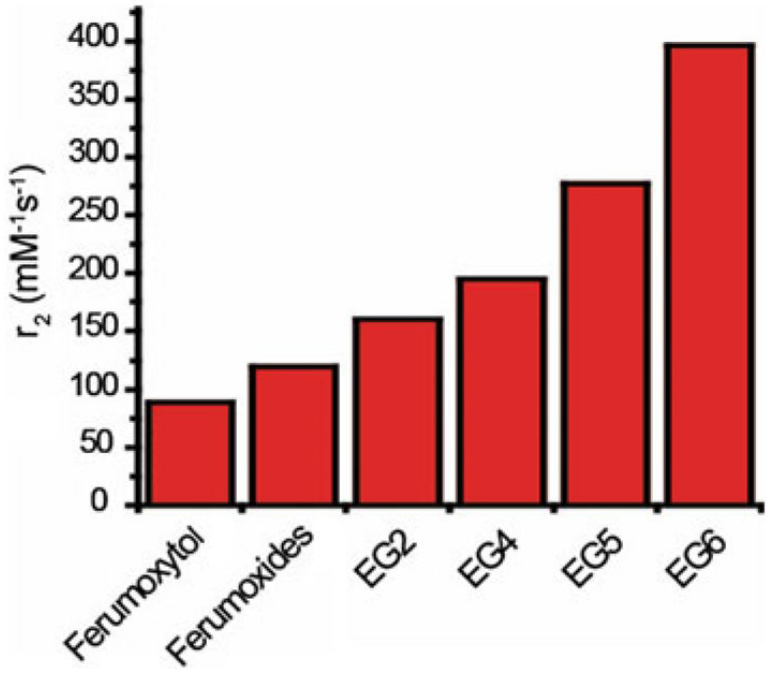

Fig. 11.

r_2 relaxivity values of 12 nm nitrodopamine-PEG functionalized Fe_3O_4 MNS with molecular weight of PEG 200 (EG2), 400 (EG4), 500 (EG5), and 600 Da (EG6) in comparison to Ferumoxytol and Ferumoxides (unpublished). It was found that the PEG coating not only provides stability but the thickness of PEG coating also affects the r_2 relaxivity of Fe_3O_4 MNS. The highest r value of 396 mM^{-1} s^{-1} with PEG 600 (EG6) was almost four times that of Feridex (Ferumoxide)

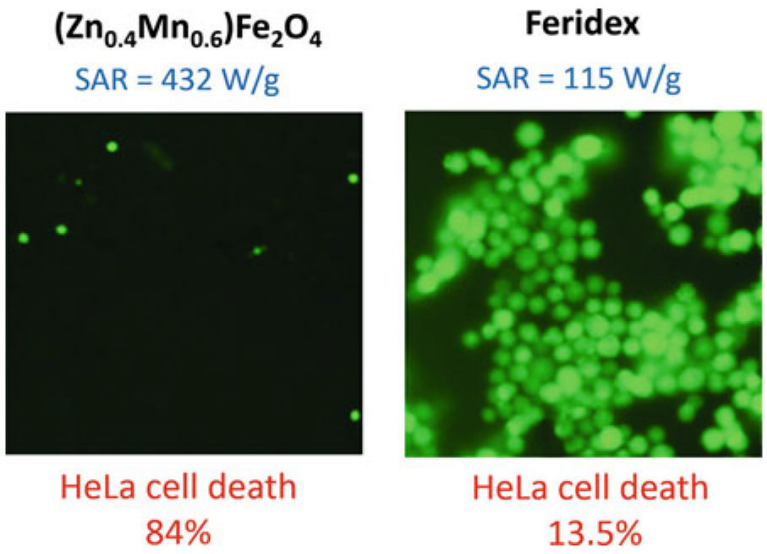

Fig. 12.

SAR values and percentage of HeLa cells killed after treatment with $(Zn_{0.4}Mn_{0.6})Fe_2O_4$ MNS or Feridex in AMF. Fluorescence microscopy images of HeLa cells treated with $(Zn_{0.4}Mn_{0.6})$ Fe_2O_4 nanoparticles (or Feridex) and stained with calcein show live cells as green fluorescence. $(Zn_{0.4}Mn_{0.6})Fe_2O_4$ MNS have shown SAR value of 432 W/g, ~4 times higher than SAR of Feridex (115 W/g) which resulted in 84.4 % death of HeLa cancer cells in comparison to 13.5 % from Feridex. Reprinted with permission from Ref. [42] Copyright © 2009 WILEY-VCH Verlag GmbH & Co. KGaA, Weinheim

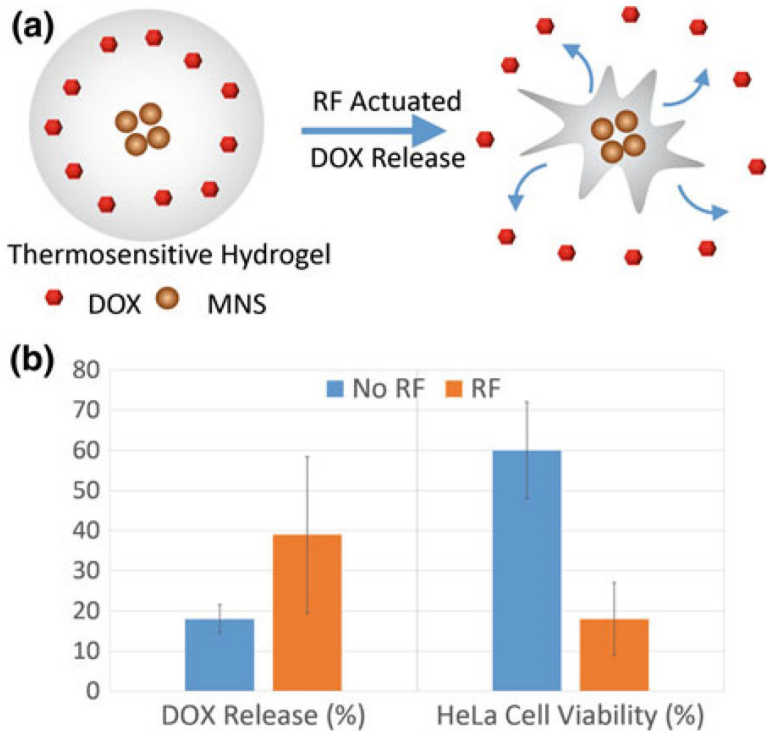

Fig. 13.

a Schematic illustration of drug (DOX) release from thermoresponsive hydrogel-MNS composite. **b** Percent DOX release and cell viability of HeLa cell lines treated with the hydrogel-MNS composite with and without external RF field [83]

Table 1

Summary of MNS with core diameter, surface coating, magnetic properties, and r_2 relaxivity

MNS core material	Core diameter (nm)	Surface coating	Magnetic moment (emu/g)	B_0 (T)	r_2 (mM^{-1} s^{-1})	References
Fe_3O_4 (Resovist)	4	Carboxy-Dextran	N/A	1.5	186	[35]
Fe_3O_4 (Feridex)	5	Dextran	45	1.5	120	[36]
Dy-SiO_2-$(Fe_3O_4)_n$	9	DMSA	N/A	9.4	397	[37]
Fe_3O_4	4–12	DMSA	25–101	1.5	78–218	[38]
Fe_3O_4	12	Nitrodopa-PEG600	N/A	1.5	396	Unpublished
Fe_3O_4	14	DSPE-mPEG1000	N/A	0.47	385	[39]
Fe_3O_4	58	DSPE-mPEG2000	132	1.5	324	[40]
$MnFe_2O_4$	6–12	DMSA	68–110	1.5	208–358	[38]
$CoFe_2O_4$	12	DMSA	99	1.5	172	[38]
$NiFe_2O_4$	12	DMSA	85	1.5	152	[38]
$Zn_{0.34}Fe_{0.66}OFe_2O_3$	5	DSPE-PEG	54.1	0.55	34.7	[41]
$Zn_{0.4}Fe_{0.6}Fe_2O_4$	15	DMSA	161	4.5	687	[42]
$Zn_{0.4}Mn_{0.6}Fe_2O_4$	15	DMSA	175	4.5	860	[42]
$Fe_{40}Co_{60}$	7	Phospholipid-PEG	215	1.5	644	[43]
Fe/Fe_3O_4	15	OAm-PEG	164	3	220	[44]
Fe/Fe_3O_4	16	DMSA	139	1.5	312	[45]
Fe/$MnFe_2O_4$	16	DMSA	149	0.47	356	[46]

r_2 transverse relaxivity; B_0 magnetic field strength; *DSPE-PEG* 1,2-Distearoyl-sn-glycero-3-phosphoethanolamine-*N*-[methoxy(polyethylene glycol)]; *DMSA* 2,3-dimercaptosuccinic acid; *OAm-PEG* oleylamine-α,ω-bis(2-carboxyethyl)poly(ethylene glycol)